



Satellite measurement of forest disturbance, recovery and deposit distribution following explosive volcanic eruptions

M.L. Udy^{a,*}, S.K. Ebmeier^a, S.F.L. Watt^{b,c}, A. Hooper^a, A. Paredes^d

^a School of Earth and Environment, University of Leeds, Leeds LS2 9JT, UK

^b School of Geography, Earth and Environmental Sciences, University of Birmingham, Edgbaston, Birmingham B15 2TT, UK

^c Birmingham Institute of Forest Research, University of Birmingham, Edgbaston, Birmingham B15 2TT, UK

^d Universidad Austral de Chile, Graduate School, PhD in Forest Sciences and Natural Resources, Valdivia, Chile

ARTICLE INFO

Keywords:

Remote sensing
Volcanic hazards
Forest disturbance
Calbuco
NDVI
Vegetation

ABSTRACT

The characteristics and extent of forest damage, and the subsequent patterns of recovery, reflect the intensity of an explosive volcanic eruption and have the potential to be a novel proxy for eruption magnitude and impact. Using satellite measurements of vegetation damage and recovery patterns, following the 2015 explosive eruption of Calbuco, Chile, we assess the impact on surrounding temperate forests and how areas impacted by different deposit types recover post-eruption. The Calbuco eruption resulted in tephra deposition over hundreds of square kilometres, pyroclastic flows extending 6 km and lahars extending 15 km. We explore NDVI derived from optical imagery (June 2013–May 2023) as well as radar backscatter and phase coherence (October 2014–June 2023) through time series analysis, clustering and estimation of recovery timescales to find patterns in forest disturbance and recovery. We find that forest damage and recovery correspond primarily with deposit type, thickness and dispersal directions. The thickest tephra deposits (> 40 cm) correlate with the most vegetation loss, so our vegetation impact maps allow us to refine the spatial mapping of tephra fall-deposit isopachs to give a revised eruption volume of 0.28 km³. Vegetation recovery rates relate to initial impact type and intensity, but also local topography, aspect and altitude. Our results demonstrate a novel application of optical and radar satellite remote sensing to determine eruption extents and magnitudes through vegetation disturbance. We show that measuring vegetation disturbance, particularly in remote and densely vegetated environments, can help refine field-based analyses in inaccessible or intensely damaged zones.

1. Introduction

Explosive volcanic eruptions can cause widespread impacts on their surrounding environment, ranging from total destruction and burial of vegetated landscapes through to minor and temporary damage (Dale et al., 2005b; Grilli et al., 2019; Major and Lara, 2013). The extent and style of damage reflects the intensity and mechanism of the driving volcanic process. Timescales and patterns of regrowth potentially reflect both the nature of initial impacts and local floral, climatic, and environmental parameters (Foster et al., 1998; Swanson and Major, 2005). Vegetation damage therefore holds potential as a novel proxy for the magnitude and nature of volcanic eruptions, enabling evaluation of the long-term environmental consequences of volcanic events. If we can calibrate the scale of vegetation damage to the nature of the driving process, this is a potential route to estimating eruption magnitudes and

deposit volumes, particularly in remote volcanic environments.

Freely available, global-coverage satellite data, provides an opportunity to systematically study relationships between volcanic eruptions and vegetation. By mapping forest recovery after a sudden disturbance event, we can gather data on the timescales and patterns of vegetation succession and ecosystem recovery. This allows us to test if, and how the post-disturbance recovery is controlled by the initial impacts (Dale et al., 2008; del Moral and Wood, 1993). If recovery timescales can be better understood, such methods hold the prospect of evaluating the impacts and magnitude of unobserved eruptions.

Here, we use the 2015 eruption of Calbuco volcano, Chile, to develop a satellite-based analysis of the impact of explosive volcanic eruptions on forest environments. This eruption is an ideal case to develop our approach, given that it occurred during an era of frequent high-resolution satellite coverage, and in a densely vegetated proximal

* Corresponding author.

E-mail address: eemu@leeds.ac.uk (M.L. Udy).

<https://doi.org/10.1016/j.jvolgeores.2024.108204>

Received 31 May 2024; Received in revised form 27 September 2024; Accepted 2 October 2024

Available online 9 October 2024

0377-0273/© 2024 The Authors. Published by Elsevier B.V. This is an open access article under the CC BY license (<http://creativecommons.org/licenses/by/4.0/>).

environment that was affected by tephra fall deposition, lahar deposits and pyroclastic density currents. We map the extent and timescale of vegetation damage and recovery detected from satellite imagery, and identify the extent of the impacts from different eruption mechanisms, using this to categorise the damaged vegetation. We calibrate our results using ground-based observations to better map out the dispersal pattern of erupted material.

1.1. Impact of volcanic eruptions on forests

The nature and timescale of volcanic impacts on vegetation are dependent on the volcanic process and its magnitude, alongside regional and local ecologies. The damage caused by large explosive eruptions can be particularly extensive, reaching thousands of square kilometres (Carey and Sigurdsson, 1989; Self, 2006). Pyroclastic density currents (PDCs) generated during explosive eruptions generally have topographically controlled distributions, destroying vegetation with which they come into contact through burning, erosion, abrasion or burial, and can singe areas adjacent to the flow deposit (Charbonnier et al., 2013). In contrast, tephra fall deposits cause less intensive damage but cover a much greater area, without topographic controls. Impacts from tephra fall deposition range from burial and branch breakage for intense and thick fallout, through to abrasion damage and defoliation for thinner and finer ash deposition (Wilson et al., 2011, 2013, 2015; Turner et al., 1997). Lahars, which occur during or after an eruption through the mixing of volcanic particles with water, are highly erosive flows that damage vegetation through channel-wall erosion and, downstream, by inundation and burial of adjacent landscapes beyond the outer flanks of volcanoes (Castruccio and Clavero, 2015).

Eruption rate, transport mechanism, deposit thickness and volume, and grain coarseness may all also affect the degree of damage or destruction of vegetation (Dale et al., 2008; Ayris and Delmelle, 2012; Swanson et al., 2013; Zobel and Antos, 1997). The temperature of deposit emplacement (for example, high temperature PDCs versus cold lahars) may be significant in controlling the style and extent of damage (Charbonnier et al., 2013). Chemical characteristics, including volatile species, soluble salts or mobile trace elements, may influence vegetation impacts and the longevity of environmental damage. For example, the presence of chlorine in volcanic gas can cause chemical toxicity in vegetation and acidification through ash deposition, contributing to vegetation loss (Swanson et al., 2013; Lowenstern et al., 2012; Dale et al., 2008). Volcanic deposits can influence vegetation patterns by affecting soil structure and composition (Ayris and Delmelle, 2012; Dale et al., 2008). In forested environments, the degree of damage is dependent on the duration and/or frequency of exposure to eruption impacts, with sustained exposure likely to impede recovery (Foster et al., 1998), as well as the mechanisms involved and their relative magnitude. Recovery timescales are influenced by local climatic and environmental conditions, the extent of environmental degradation (e.g. hydrographic changes, soil burial) caused directly by the eruption, and the nature of the local forest ecosystem. For example, regrowth and succession timescales in tropical forests can be very rapid in comparison to high-latitude environments (del Moral and Wood, 1993; Foster et al., 1998; Gillman et al., 2015). Patterns of damage can also vary between eruption processes. Tephra fall deposits or blasts typically produce sectoral patterns decaying away from the eruption site. In contrast, lava flows, lahars and PDCs have a more linear impact pattern, mainly influenced by topography, with similar degrees of damage along the main transport pathway (Foster et al., 1998). Volcanic gases contribute to vegetation damage, both during an eruption or via passive emission, and either indirectly (e.g. soil alteration or acid rain) or directly (e.g. direct gas exposure leading to plant death) (Lowenstern et al., 2012; Smith, 1981; Delmelle, 2003; Gerlach et al., 2001).

The disturbance pattern has an influence on the post-eruption recovery of vegetation (Foster et al., 1998). Linear disturbances from lahars, lava flows and PDCs, may be adjacent to healthy, relatively

undisturbed and mature vegetation, with a sharp boundary. This influences recovery and succession at the margins of damaged areas, with nearby seed sources promoting regrowth within narrow damage zones (Foster et al., 1998). Conversely, sectoral patterns of disturbance from blasts or tephra fall are characterised by gradational damage patterns. The most intensely damaged parts of these regions may be slow to recover due to their distance from undamaged vegetation and the severity of damage (Dale et al., 2008), while marginal zones may recover rapidly. Surviving plant matter is key to recovery as it is essential to instigate regrowth (Franklin et al., 2000; Franklin, 1990; Dale et al., 2005a). Post-disturbance vegetation recovery rates can vary, and may be exponential or linear depending on vegetation type, the stage of regrowth and how the recovery is measured (Viedma et al., 1997; de Jong et al., 2012; Buitenwerf et al., 2018; Bonesmo and Skjelvg, 1999; Bastos et al., 2011).

1.2. Estimation of forest properties from satellite data

Satellite data provides global information about the state of vegetation (Dorigo et al., 2007). Forest characteristics used to assess health and growth rate, such as tree height, tree diameter and wood density, are not directly measurable from satellite imagery (Brown et al., 1989). However, there are well established relationships between many satellite-derived metrics and forest-derived physical characteristics (Mitchard et al., 2009; Santin-Janin et al., 2009). The relationship between the optical reflectance spectrum (between 400 and 15,000 nm wavelength, containing the visual, infrared and thermal bands) and vegetation is relatively well understood. The reflectance of a forest largely depends on characteristics of leaves and soil, including leaf structure, chlorophyll content and soil moisture, giving a direct indication of plant health (Jacquemoud and Baret, 1990). However, the application of optical data is limited by cloud cover or regions of high biomass where the signal saturates (Song, 2013).

Satellite radar, dominantly Synthetic Aperture Radar (SAR), (~3–100 cm wavelength) is not limited by time of day or cloud cover (Kim et al., 2012). Radar can also return information about vegetation heights due to its longer wavelength, allowing it to penetrate through the top vegetation layer (Treuhft et al., 1996; Balzter, 2001). Different radar wavelengths interact with different sized scatterers and reach different depths of the canopy. Generally, smaller scatterers are near the top and larger scatterers near the bottom of the canopy, and increasingly longer wavelengths are therefore able to penetrate through the canopy down to the forest floor (Woodhouse, 2017). Vegetation can be monitored using radar backscatter, phase coherence and polarimetry (Treuhft et al., 1996; Askne et al., 1997; Evans et al., 1988). Backscatter in particular, is used to estimate forest biomass, on the basis of empirical relationships (Woodhouse, 2017; Mitchard et al., 2009) that are strongest at longer wavelengths (Woodhouse, 2017; Mitchard et al., 2009).

1.3. Volcanic eruption impacts on forests

The impact of explosive eruptions on vegetation has been investigated in detail at a handful of historical eruption sites (e.g. Mt. St Helens, USA, 1980; Unzen, Japan, 1990–1995; Chaitén, Chile, 2008; Cordón Caulle, Chile, 2011) (del Moral and Wood, 1993; Dale et al., 2005b; Martin et al., 2009; Lai et al., 2022; Swanson et al., 2013; Biass et al., 2022; Easdale and Bruzzone, 2018; Smathers and Mueller-Dombois, 1972). There have also been regional investigations of ecosystem structures in eruption-impacted regions (e.g. Grishin et al., 1996) and global studies of specific impact types (e.g. tephra fall; (Biass et al., 2022; De Schutter et al., 2015; Easdale and Bruzzone, 2018). Studies that rely on field measurements, such as ash thicknesses or vegetation samples, tend to capture only one or a few points in time after an eruption (Martin et al., 2009; Swanson et al., 2013). A subset of studies use tree ring data to understand the impact of volcanic eruptions on forests, demonstrating at a number of volcanoes (including Parícutin,

Colima and Tacana) that ashfall inhibits growth of trees during eruption periods (Biondi et al., 2003; Carlon Allende et al., 2020; Carlon Allende et al., 2022). Tree rings have also been used to identify lahar activity and pre-eruption enhanced growth through measurement of stable oxygen isotopes in tree rings (Franco-Ramos et al., 2016; Seiler et al., 2021).

Satellite studies rely primarily on metrics derived from optical imagery (Li et al., 2018; De Schutter et al., 2015; Easdale and Bruzzone, 2018; Lai et al., 2022; Teltcher and Fassnacht, 2018; Biass et al., 2022; Balzter, 2001). While satellite radar data are widely used to investigate effusive and explosive volcanic deposits (Dualeh et al., 2021; Ebmeier et al., 2012; Jung et al., 2016; Babu and Kumar, 2019), the focus is primarily on volcanic flow deposits (Head et al., 2012; Macorps et al., 2023) and studies can avoid vegetated areas, as they are a source of phase decorrelation (Zebker et al., 1992).

1.4. The 2015 eruption of Calbuco

Calbuco is an andesitic arc stratovolcano located in the Southern Chilean Andes at 41.3° South. The land to the west is agricultural, but the flanks of the volcano and the land to the east and south are densely forested, and relatively undisturbed by human activity (Fig. 1). The volcano has an elevation of 1974 m and is in a temperate broadleaf and mixed forest, characterised by high species diversity and high endemism (Olson et al., 2001; Echeverria et al., 2006). The climate at Calbuco is temperate oceanic, resulting in heavy rainfall throughout the year but with relatively warmer and drier summers (Peel et al., 2007). In the 100 years prior to the VEI 4 2015 eruption, Calbuco experienced explosive eruptions in 1972, 1961, 1945, 1932, 1929, 1927, and 1917; all of these had lower estimated magnitudes (VEI 3 or lower) than the 2015 eruption (Global Volcanism Programme, 2015; Romero et al., 2016). Historical

eruptions have involved tephra fall deposition, lava flows, lahars and PDCs (Global Volcanism Programme, 2015). Although these previous eruptions have impacted the forested flanks of Calbuco, their lower magnitude means that their footprint was likely smaller than the 2015 event, and the 43 year hiatus in activity since the previous eruption has provided a long recovery period. There are detailed independent observations of the 2015 eruption, with some mention of specific damage to vegetation (Castruccio et al., 2016; Romero et al., 2016; Van Eaton et al., 2016).

The 2015 eruption of Calbuco began on the evening of the 22nd of April and involved two main explosive pulses. The initial pulse began soon after the start of the eruption and lasted ~90 min, generating a 15 km high plume dispersed on an azimuth of 48°. A second, more intensive pulse followed on 23rd April, lasting six hours and generating a >15 km high plume, dispersed on an azimuth of 55°. Umbrella cloud expansion patterns suggest slightly different dispersal axes, of ~35° for the first pulse, alongside a more northerly component, and ~50° for the second pulse (Van Eaton et al., 2016), broadly consistent with the dispersal axes constructed from tephra deposits in Castruccio et al. (2016). Continued venting, with columns <2 km high, occurred over several days, with a further pulse and 4 km high column on 30th April (Romero et al., 2016). The eruption caused tephra fall to the NE of the volcano, as shown by the isopachs in Fig. 1 from Romero et al. (2016). Romero et al. (2016) identify four units in the tephra fall deposits, interpreting the two larger-volume central layers as corresponding to the two main eruption pulses, with the bounding layers representing activity leading into and out of these phases. Dispersal patterns of the two thickest layers are consistent with the satellite-observed dispersal directions, although constraints on very proximal depositional patterns are limited due to inaccessibility on the flanks of

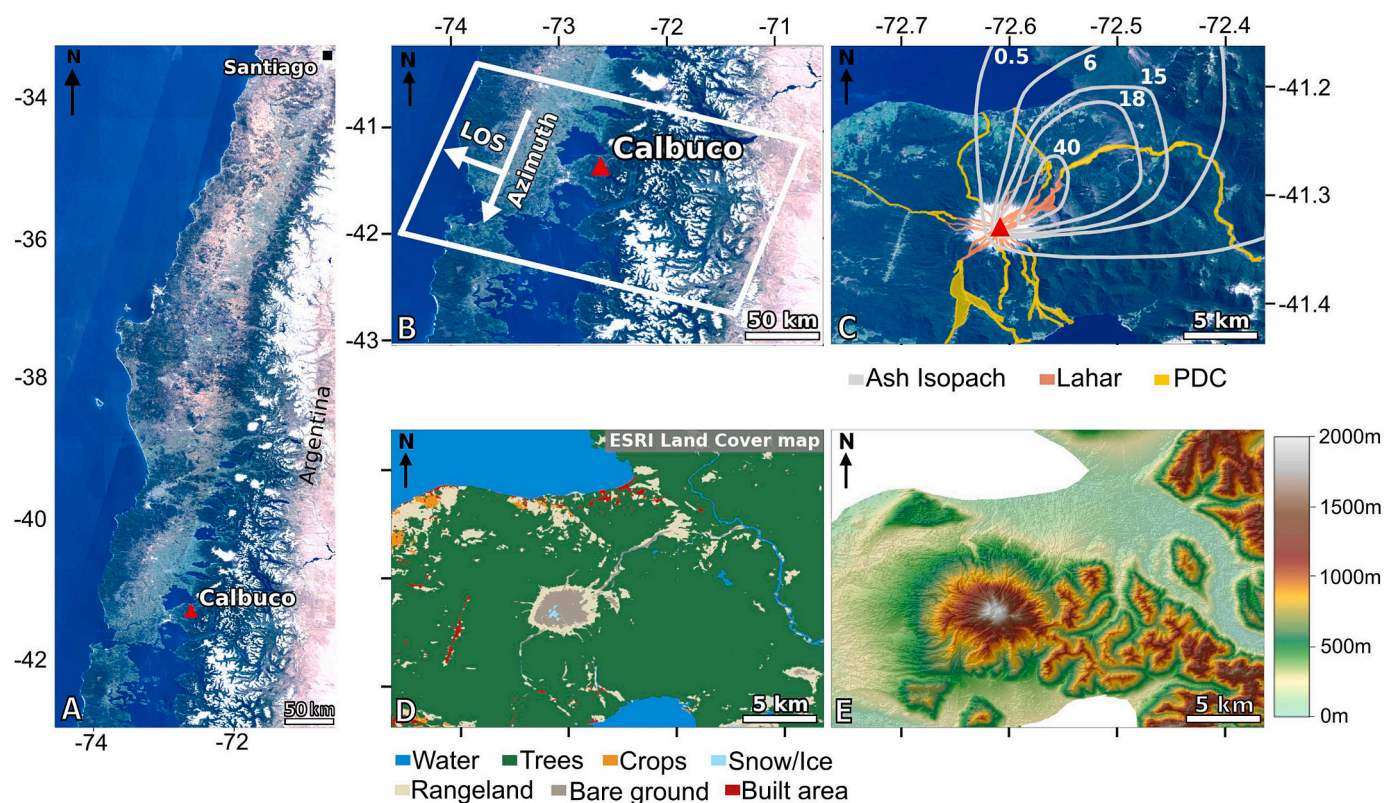


Fig. 1. A) Sentinel-2 optical satellite image showing the location of Calbuco within Chile, and in relation to the capital of Santiago B) Sentinel-2 optical satellite image showing the location of Calbuco with the Sentinel-1 tile used, with the line of sight and azimuth direction shown. C) Sentinel-2 optical satellite image showing the location of PDC, lahar and tephra deposits from a combination of Hayes et al. (2019); Mella et al. (2015); Castruccio et al. (2016); Romero et al. (2016) and our own mapping. D) ESRI land cover map of Calbuco in 2022. E) A TanDEM-X digital elevation model of Calbuco. The geographic extents of panel D and E are the same as panel C. Where necessary the keys required are below their relevant panel.

Calbuco. The total tephra fall deposit volume was estimated at 0.27 km^3 (Romero et al., 2016) (a separate estimate of 0.34 km^3 is given by Castruccio et al. (2016)), with $\sim 38 \%$ of the volume erupted from the first pulse, and $\sim 46 \%$ from the second pulse (the remaining volume being erupted by subsequent activity) (Romero et al., 2016). Pyroclastic flows, channelised within radial valleys, occurred on the N, NE, W and S flanks of the volcano, as seen in Fig. 1 (based on previous channel deposit maps and our own satellite observations), reaching up to 8 km from the vent and with a total bulk volume of $\sim 0.07 \text{ km}^3$ (Global Volcanism Programme, 2015; Castruccio et al., 2016; Romero et al., 2023). Concentrated PDCs were generally channelised along river valleys, with more extensive impacts to a distance of 4 km NE of the vent. Within areas impacted by concentrated PDCs, deposits reached several metres in thickness, and vegetation death occurred through toppling, burial, and charring, with flow temperatures estimated at $\sim 500^\circ\text{C}$. Marginal zones, scorched by dilute PDCs, did not experience total death of vegetation, with surviving trees subsequently re-sprouting (Romero et al., 2023). Syn-eruptive lahars extended down river channels beyond the limits of PDC deposits, extending to coastal or lake outflows to the N, S and E (Global Volcanism Programme, 2015; Castruccio et al., 2016). Following the final explosive eruption episode on the 30th of April, low level activity continued throughout May until the eruption was deemed to be over on the 26th of May (Global Volcanism Programme, 2015).

2. Methods

2.1. Data

2.1.1. Optical imagery

We extracted surface reflectance data from Sentinel-2 and Landsat 8 through Google Earth Engine. Sentinel-2, comprising Sentinel-2a and Sentinel-2b, has a 5 day repeat time with spatial resolution of 10 m and Landsat 8 has a 16 day repeat time with 30 m spatial resolution. The level 2 data used in this work have been atmospherically corrected (Main-Knorn et al., 2017; Vermote et al., 2016). We then used Google Earth Engine to remove any acquisitions with more than 40 % cloud cover. A cloud mask using the pixel Quality Assurance band (Foga et al., 2017; Main-Knorn et al., 2017) was applied to the remaining dataset, and any images that still contain clouds were removed manually. This resulted in a dataset of 79 Landsat 8 images and 162 Sentinel-2 images spanning from June 2013 to May 2023.

2.1.2. Radar imagery

We used radar images obtained from Sentinel-1 (from descending track 83), a satellite constellation that consisted of Sentinel-1a and Sentinel-1b (until Sentinel-1b failed on the 23rd of December 2021). Sentinel-1 uses a C band (6 cm) synthetic aperture radar (SAR), with a revisit time of 6 days (when 1a and 1b are combined) and a geometric resolution of $5 \text{ m} \times 20 \text{ m}$ in interferometric wide swath (IW) mode, which is the default mode over land (Torres et al., 2012). We used 201 Single Look Complex (SLC) images from October 2014 until June 2023,

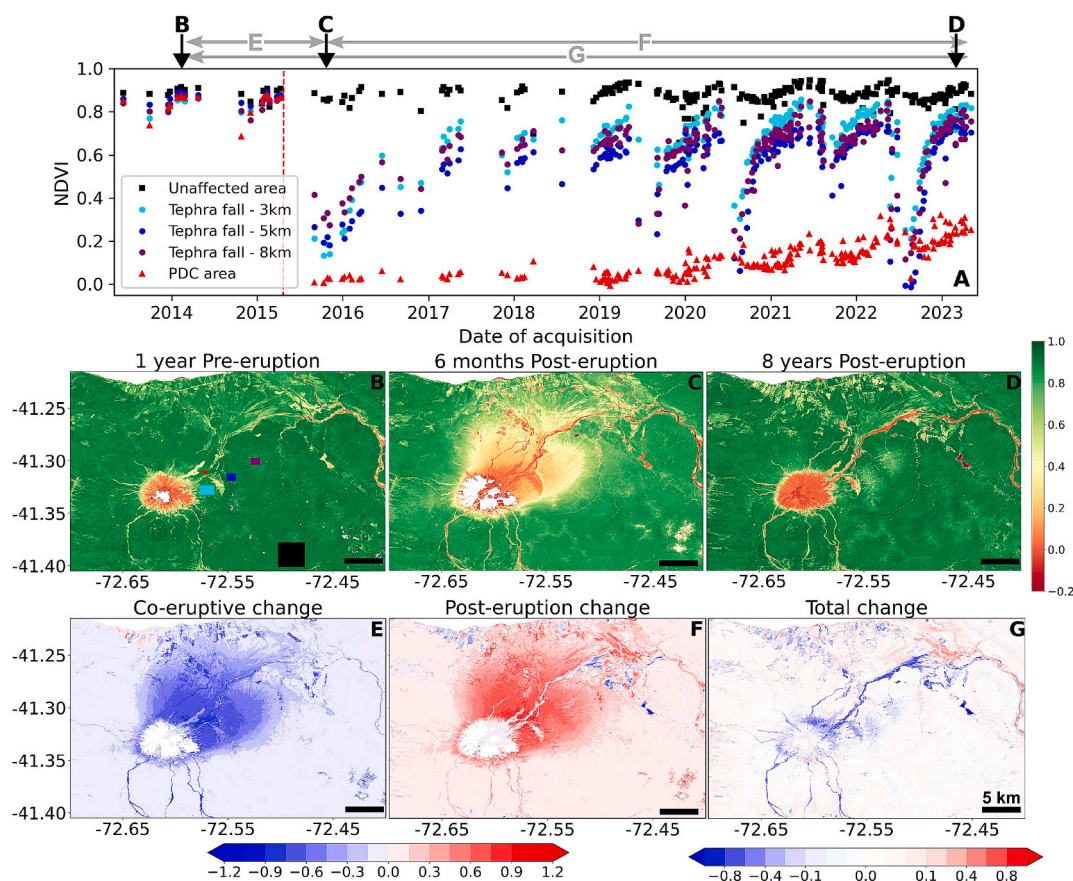


Fig. 2. A) NDVI time series of 1 unaffected area (black), 3 tephra impacted areas (at 3, 5 and 8 km from the vent) in light blue, dark blue and purple respectively and 1 PDC affected area (red). Time of eruption is indicated by the red dotted line. We generate time series by calculating the average NDVI value within the defined study area. For a given acquisition, if any study area has $>10 \%$ of pixel values (likely due to clouds) it was removed from the analysis. B) Pre-eruption NDVI image (26/02/2014) highlighting the location of the 5 study areas, C) Post-eruption NDVI image (27/10/2015), D) post-recovery NDVI image (02/02/2023), E) NDVI difference image demonstrating co-eruptive change (26/02/2014–27/10/2015), F) NDVI difference image demonstrating post-eruption change (27/10/2015–17/02/2023) G) NDVI difference image demonstrating total change in NDVI (26/02/2014–17/02/2023).

accessed through the Nasa ASF data portal. We limited our analysis to single polarisation (VV), as dual polarisation was not available for all acquisitions. The SLCs are geo-referenced, focused SAR images in slant range geometry.

2.1.3. Study areas

Throughout this article, we use five sites around Calbuco (Fig. 2) to illustrate the impact of different volcanic deposits on vegetation and recovery rates. We selected three areas impacted by tephra fall, one impacted by channelised PDC deposition and one area not directly impacted by the eruption material. The study sites have been selected to only contain pixels impacted by the specified deposit type, and the mean pixel value is then taken for each study area. The style of initial impact was independently verified using reported post-eruption observations (Global Volcanism Programme, 2015; Hayes et al., 2019; Van Eaton et al., 2016; Romero et al., 2016). A detailed description of these study areas is provided in section A1 in the appendix.

2.2. Optical remote sensing

We used the optical imagery to calculate Normalised Difference Vegetation Index (NDVI), a widely used index that utilises the relationship between chlorophyll reflectance in the infrared and red spectral bands to assess quantity and health of vegetation (Santin-Janin et al., 2009; Myneni et al., 1995; Veloso et al., 2017; Goetz et al., 2006; Bai et al., 2008; Tian et al., 2015). We chose this index over alternatives such as the normalised burn ratio or enhanced vegetation index because it is a traditional vegetation index that has been proven to be effective in showing vegetation disturbance and recovery, particularly for characterising post-fire recovery (Veraverbeke et al., 2012; Chen et al., 2011; De Schutter et al., 2015). We expect it will perform better at differentiating volcanic impact types, and assessing vegetation health, rather than just structural changes, as it is chlorophyll sensitive and better suited to areas of changing topography (Roy et al., 2006; Matsushita et al., 2007; Lai et al., 2022).

NDVI values range from -1 to 1 ; dense, healthy vegetation is indicated by strong positive values, due to high near infrared reflectance and low red reflectance associated with chlorophyll containing cells, while values close to zero or negative indicate non-vegetated areas. We generated time series of NDVI to highlight areas of significant change and to capture the footprint of volcanic deposits (De Schutter et al., 2015; Gouveia et al., 2010; Marzen et al., 2011; Gouveia et al., 2009; Michener and Houhoulis, 1997; Lu et al., 2012; Chou et al., 2009; Easdale and Bruzzone, 2018).

2.3. Satellite radar backscatter and coherence

SAR sensors emit an electromagnetic pulse and measure the returned signal that is directed back from the ground (backscatter). We estimated backscatter from the Sentinel-1 dataset using the GAMMA remote sensing software (Werner et al., 2018) following the processing steps outlined by Werner et al. (2000), summarised by fig. A.1. We limited our analysis to five bursts (2–6, middle swath, descending track 83). The SLC was deramped to account for the Doppler centroid generated by the TOPS ScanSAR mode (Yagüe-Martínez et al., 2016), and the 5 bursts were mosaicked together and co-registered to a common date (23/10/2014). We multi-looked over a window size of 10×2 in the range and azimuth direction respectively to produce a multi-look intensity image (MLI) (Lee et al., 1994). We performed terrain corrections and radiometric calibrations using the TanDEM-X digital elevation model to mitigate for the impact of topography on backscatter, remove geometric and radiometric image distortions and decrease sensitivity to fluctuations in incidence angle (Dualeh et al., 2021; Meyer et al., 2015; Small, 2011). We geocoded the images using the same DEM to produce 201 backscatter images. We then produced time series of backscatter for the 5 study areas by averaging the pixel values. We produced backscatter

difference maps to view the changes associated with the eruption impacts and post-eruption regrowth. We constructed interferograms for the sequential 24-day pairs within our dataset and estimated phase coherence for each pair using a 5×5 sliding window (Hanssen, 2001). We chose 24-day coherence due to the temporal resolution of our dataset, in order to maximise the number of coherence images we could use for cluster analysis. Interferometric phase coherence is commonly characterised by estimating the complex correlation coefficient between two SAR images and ranges from 0 (completely incoherent) to 1 (completely coherent) (Just and Bamler, 1994). Rapidly changing surfaces, like vegetation, will have low coherence (values close to 0) compared to more stable scattering surfaces, like bare ground, which have high coherence (values closer to 1) (Zebker et al., 1992; Babu and Kumar, 2019; Dualeh et al., 2021). Damage to the vegetation due to volcanic deposits should be detected by changes in coherence, with vegetation loss resulting in a more stable surface and higher values of coherence. We produced time series of coherence, and use the convention of plotting coherence for each interval as the first date in the pair.

2.4. Cluster analysis

We generated a time series for each of the pixels in the NDVI, backscatter and coherence datasets and used k-means clustering (Likas et al., 2003) to group the pixels sharing common trends. Before clustering we downsampled the images by a factor of 2 in both the azimuth and range directions, and removed acquisitions that have more than 10 % NaNs. We removed any remaining NaNs by 2D linear interpolation, followed by zero-padding any regions unable to be interpolated. We found the optimal number of clusters for each dataset through experimentation and iterative refinement. For each dataset the k-means algorithm was run 10 times with different centroid seeds.

3. Results

3.1. NDVI

We show the changes in NDVI with time in Fig. 2, for five selected study sites representing different initial impacts. Areas impacted by tephra fall deposition (Fig. 2 panels A and B) all show an immediate decrease in NDVI of up to 85 %, followed by a relatively rapid initial recovery until around 2018, when the rate of recovery slows but continues to increase steadily towards pre-eruption values. The magnitude of the co-eruptive decrease in NDVI correlates with the thickness of ash deposition (and the distance from the vent), as expected. However, the initial rate of recovery is highest for the region closest to the volcano. By early 2017, this region has higher NDVI values than the other two tephra-impacted areas, by around 15 %. This is in contrast to what would be expected if recovery rate were simply proportional to tephra thickness. The PDC-impacted area shows a different trend, immediately after the eruption NDVI decreases by 99 %. Compared to the tephra-fall areas, there is little recovery in NDVI until 2019, after which it increases linearly. By 2023, the NDVI in channels affected by PDCs is still well below pre-eruption values.

NDVI change is shown in panels E-G for three periods spanning the eruption. Panel E shows the change in NDVI from a year pre-eruption (26/02/2014) to 6 months post-eruption (27/10/2015). The change here is likely to be dominated by co-eruptive impacts, and NDVI change is negative for all areas impacted by the eruption. This decrease is most intense in the vicinity of the volcano and towards the north-east, correlating closely with the area of thickest (and coarsest) tephra fall deposition (Romero et al., 2016). This gradation in NDVI (plotted in increments of 0.15) corresponds well to previous tephra-fall deposit isopach maps (Romero et al., 2016; Hayes et al., 2019), but highlights finer scale spatial variation than is evident in field-based ash-thickness reconstructions (which are extrapolated from a small number of point measurements). Panel F shows the post-eruption recovery in NDVI over

a period of 7 years and 4 months (until 17/02/2023). Over this time, NDVI increases with a magnitude corresponding closely to the initial decrease in Panel E. There are some differences at a finer scale, implying that recovery may also be influenced by local factors, such as topography, slope aspect, altitude or soil conditions. Despite greater initial impacts, the forests affected by the thickest tephra fall deposits have recovered to similar NDVI values as those areas affected by thinner deposits over the 7 year timescale. Panel G shows the total change in NDVI from a year pre-eruption (26/02/2014) until almost 8 years post-eruption (17/02/2023). The overall change throughout the image is close to zero, but isolated patches to the north east of the volcano still show the imprint of tephra-fall. We note that these remaining patches of lower NDVI are discontinuous and do not simply correspond to the extent of initial NDVI reduction. The strongest residual impact on vegetation is in the channels affected by both PDC and lahar deposition.

Fig. 3 illustrates the relationship between tephra-fall deposition and NDVI, and shows 8 areas at increasing distances along a line of approximately 60° azimuth, chosen to align with the dispersal axis of tephra deposited from the most intense phase of the eruption (Romero et al., 2023). With increasing distance, the co-eruptive decrease in NDVI gets smaller until around 16 km, beyond which there is no clearly detectable eruption impact in the NDVI. Based on post-event mapped isopachs, this distance equates to around 15 cm of ash deposition (Hayes et al., 2019; Romero et al., 2016). Within this 16 km transect, the post-eruption recovery of NDVI is slowest in the most proximal areas, but follows a similar recovery trend at all sites, of a rapid initial increase followed by a steady, slower increase back towards pre-eruption values. Locations beyond 10 km return to pre-eruption values within 2 years

following the eruption. The three locations closest to the volcano take substantially longer and are yet to fully recover to pre-eruption values. The impacts of tephra fall within a distance corresponding to the ~20 cm isopach are more substantial and persistent than zones beyond this thickness, with an average NDVI decrease of 0.58 and minimum recovery time of 5 years. Within distances of 10 km, there is a strong seasonal signal evident in the NDVI recovery period, particularly from 2020 onwards. This seasonality signal appears to strengthen as the forest recovers (but we note that winter data gaps in the earlier recovery period may obscure seasonality signals from 2015 to 2020). We speculate that this could relate to a stronger seasonal growth signal from early successional vegetation on the forest floor, following canopy damage, rather than a tree-dominated mature forest signal from the relatively less damaged region beyond 10 km.

3.2. Backscatter

The backscatter data has been referenced to an average background value of the mean backscatter for all pixels excluding the volcano and the areas to the north and east (the directly impacted areas). Radar backscatter is most strongly affected where there is a change from volumetric to surface scattering (e.g., due to forest canopy loss or changes to local slope). Immediately following the eruption, there is a sharp increase in backscatter wherever vegetation was damaged (Fig. 4), with the greatest increase in the most proximal areas, affected by tephra fall deposition. Following this, all affected locations show a decline in backscatter, which had not returned to pre-eruption values consistently by 26/06/2023. The variation in the backscatter values after the

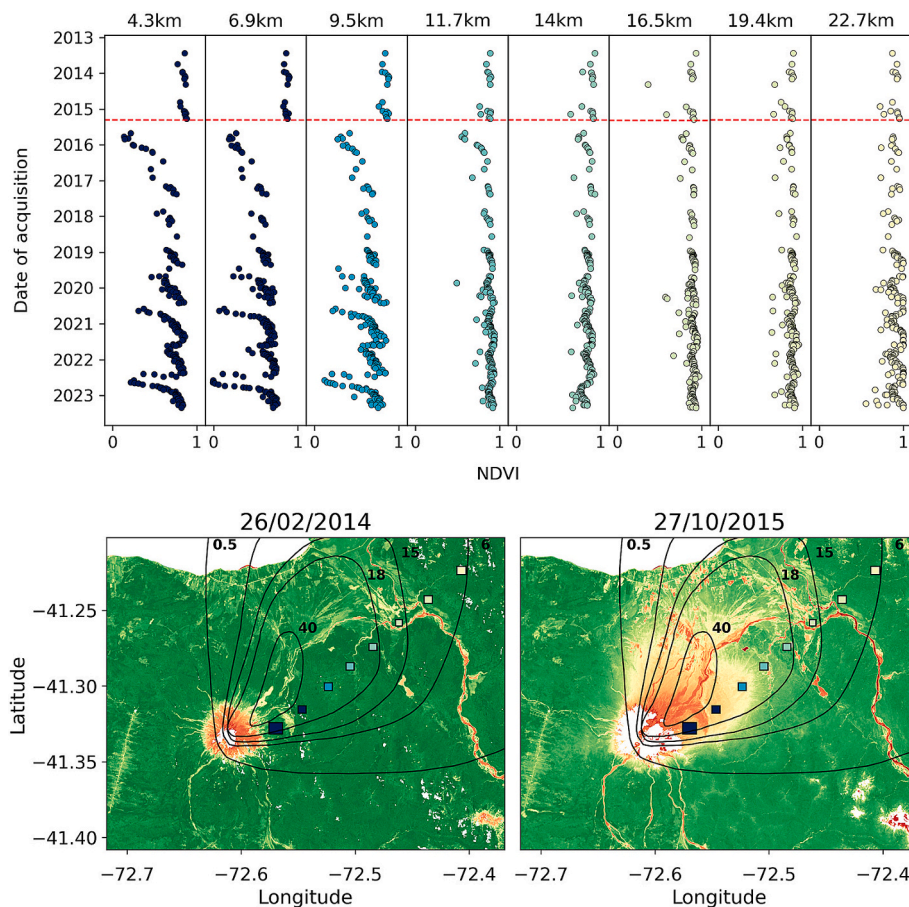


Fig. 3. A) Time series of NDVI at 8 locations of increasing distance from Calbuco, the eruption marked by a red dotted line, B) pre-eruption NDVI image (26/02/2014) with the 8 locations indicated and the ash isopachs from Romero et al. (2016), C) post-eruption NDVI image (27/10/2015) showing the locations and ash isopachs.

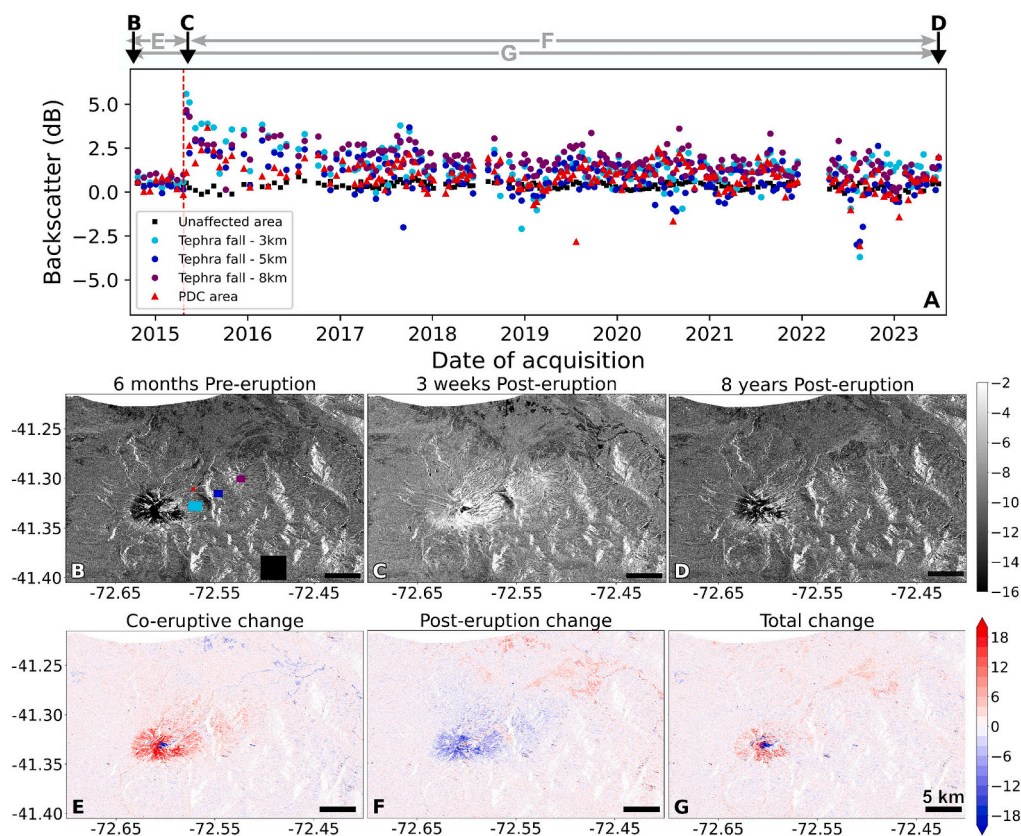


Fig. 4. A) Backscatter time series for 5 areas around Calbuco, the backscatter is referenced to the average value of the image with the volcano and directly impacted areas removed. If any box in a given acquisition has values for $>10\%$ of the pixels it was removed from the analysis. B) pre-eruption backscatter (23/10/2014) image showing the study area locations, C) post-eruption backscatter (15/05/2015) image, D) Post-recovery backscatter (02/06/2023), E) Backscatter difference showing co-eruptive change (23/10/2014–15/05/2015), F) backscatter difference showing post-eruption change (15/05/2015–02/06/2023), G) total change backscatter (23/10/2014–02/06/2023).

eruption onset is greater than before the eruption. The variance decreases with recovery, but does not reach pre-eruption values (Appendix fig. A.2). Panel E in Fig. 4 shows an increase in backscatter around the vent and a slight increase towards the north east, broadly corresponding to the area affected by thickest tephra fall deposition (isopachs of >30 cm), but without the clear gradation evident in NDVI. The negative backscatter difference to the NE of the vent (panel F) correlates with the initial positive increase, again showing a less gradational pattern to that observed in NDVI. Recovery trends are less evident in the backscatter, but some increase is evident in PDC channels and proximal tephra zones, but with no discernible difference between these two impact types in terms of backscatter recovery rates. This is likely due to the loss of vegetation or changes to its structure, which lead to minor alterations to the scattering pathway, resulting in backscatter changes in areas affected by both tephra fall and PDC deposits. The overall change in average backscatter is minimal, with the strongest changes occurring close to the volcano. These changes show an offset concentric pattern, which may be due to structural changes at the vent or long-term changes in snow and ice cover.

3.3. Coherence

Changes in phase coherence for a 24-day temporal baseline are shown in Fig. 5, plotted at the time of the first image in the pair, for the same study areas assessed using NDVI and backscatter (Panel B). The pre-eruption correlation values are very low (<0.3) over the undisturbed forest. At the time of the eruption (red dotted line) they decrease to 0–0.1, due to the phase changes associated with the eruption deposits,

before increasing steadily to 0.4 by early 2016, due to vegetation loss and an increase in exposed ground surfaces. From mid-2016 onwards the coherence values in the channels where PDCs and lahars have removed all vegetation are generally higher than those areas affected by tephra fall deposition. In areas affected by tephra fall, there is a decrease in coherence values lasting several years, returning to pre-eruption values by 2022. This contrasts with the NDVI, where tephra fall impacted areas generally reached pre-eruption values after 5 years. Within the channels, coherence values remain high but very variable.

We generate coherence difference maps (Fig. 5 panels E–G) to highlight changes in coherence throughout the eruption and recovery process, and to show how coherence evolved from pre-eruption to 8 years post-eruption. The eruption of Calbuco caused an immediate drop in coherence in most areas around the volcano (Fig. 5 panel E), but also in areas known not to have been affected by the eruption (e.g., to the south), such that the eruption-affected area is not clearly delineated. However, during the six-year post-eruption period (Fig. 5 panel F) there are strong increases in coherence, particularly in channels around the volcano and some patches to the N and E. These patches match those areas affected most strongly by tephra fall in the NDVI data, but other patches are also present to the SE, which were less discernible in the NDVI data. The total change in coherence from pre-eruption to post-eruption is around zero in most of the surrounding forest, with increases in coherence limited to a concentric zone around the volcano summit, within channels, and within a small proximal zone towards the NE (Fig. 5 panel G) where damage to the forest was most severe.

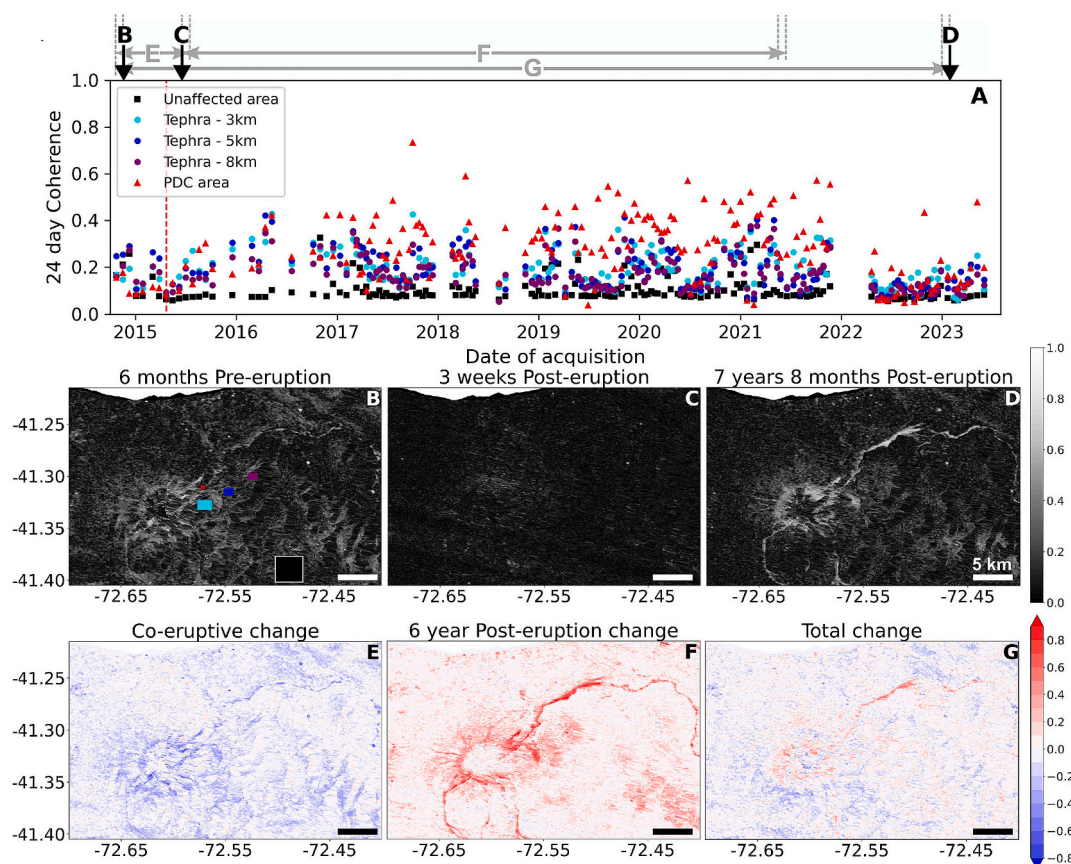


Fig. 5. A) Time series of 24-day coherence at 5 locations around Calbuco, the date is taken as that of the first image in the coherence pair B) pre-eruption (23/10/2014–16/11/2014) coherence image showing the study area locations C) post-eruption coherence image (15/05/2015–08/06/2015) D) a post-recovery coherence image (28/12/2022–21/01/2023) E) Co-eruptive coherence change formed by a pre-eruption coherence image (23/10/2014–16/11/2014) and a post-eruption coherence image (15/05/2015–08/06/2015) F) post-eruption coherence change from a post-eruption coherence image (15/05/2015–08/06/2015) and a 6 year post-eruption coherence image (01/05/2021–25/05/2021) G) Total coherence change from pre-eruption (23/10/2014–16/11/2014) to 8 years post-eruption (28/12/2022–21/01/2023).

3.4. Classification of impact zones

We perform k-means cluster analysis for all pixels in our NDVI and 24-day phase coherence datasets, grouping pixels with similar time series to produce clusters. We found that our backscatter time series were too noisy to identify meaningful clusters (Appendix fig. A.3). During the period spanning the eruption (26/02/2014–09/02/2016), NDVI forms 8 clusters with similar impact trajectories that strongly delineate a radiating sectoral damage pattern similar to known tephra fall deposit patterns in Fig. 6 (panels A and B). During the post-eruption recovery period (12/03/2016–13/04/2023), the cluster analysis also forms 8 clusters, but reveals a different spatial distribution. Cluster distribution is dominated by channels and higher topographic areas, rather than a sectoral pattern (Fig. 6 panels C and D). We cluster the coherence time series spanning the post-eruption period from 27/02/2016 to 12/01/2019, due to a loss of coherence over the co-eruptive period, forming 6 clusters (Fig. 6 panels E and F). This outlines an impact pattern NE of the volcano that is consistent with the NDVI clustering but less spatially extensive, and emphasises channels. Linear changes to the west of Calbuco, grouped within the same clusters, are due to forest clearing that occurred during the eruption and recovery period. One cluster of the coherence time series (labeled ‘tephra zone c/topography’) does not correspond to any spatial pattern of deposits but aligns with areas of higher elevation (see Fig. 1 panel E). Local environmental factors related to altitude, topography or variations in vegetation type, could explain this cluster in the coherence data.

4. Discussion

4.1. The impact of the 2015 Calbuco eruption on vegetation

Different aspects of the Calbuco 2015 eruption and recovery of the surrounding forests are captured by optical and radar imagery. The immediate eruption impacts are clearest in a sudden NDVI decrease over all areas affected by PDCs, lahars and tephra fall up to approximately 15 cm deposit thickness (Fig. 2 F, appendix fig. A.4). While the decrease in NDVI effectively shows gradational changes corresponding to eruption impact intensity, backscatter values only pick out high magnitude change within a few kilometres of Calbuco’s summit. Part of this backscatter increase, perhaps related to slope changes close to the vent, remains 8 years post-eruption. Some backscatter increase in channels is also evident due to vegetation loss or structural changes (Fig. 4 E, F, G, appendix fig. A.4). The increase in backscatter variance from pre-eruption to post-eruption may be due to structural changes to the vegetation, and would be consistent with the vegetation coverage becoming less homogeneous, a change that may not be apparent in the NDVI or the coherence. The forests around Calbuco typically have relatively high backscatter and very low coherence values. As such, the loss of vegetation, resulting in the creation of temporarily stable surfaces in the channels affected by both PDCs and lahars, is strongly highlighted by a post-eruption increase in coherence, which is also evident in NDVI. Similar coherence mapping also identifies the areas of thickest tephra deposition, but without the fine gradation evident in the NDVI dataset. While the optical data provides a detailed view of vegetation health

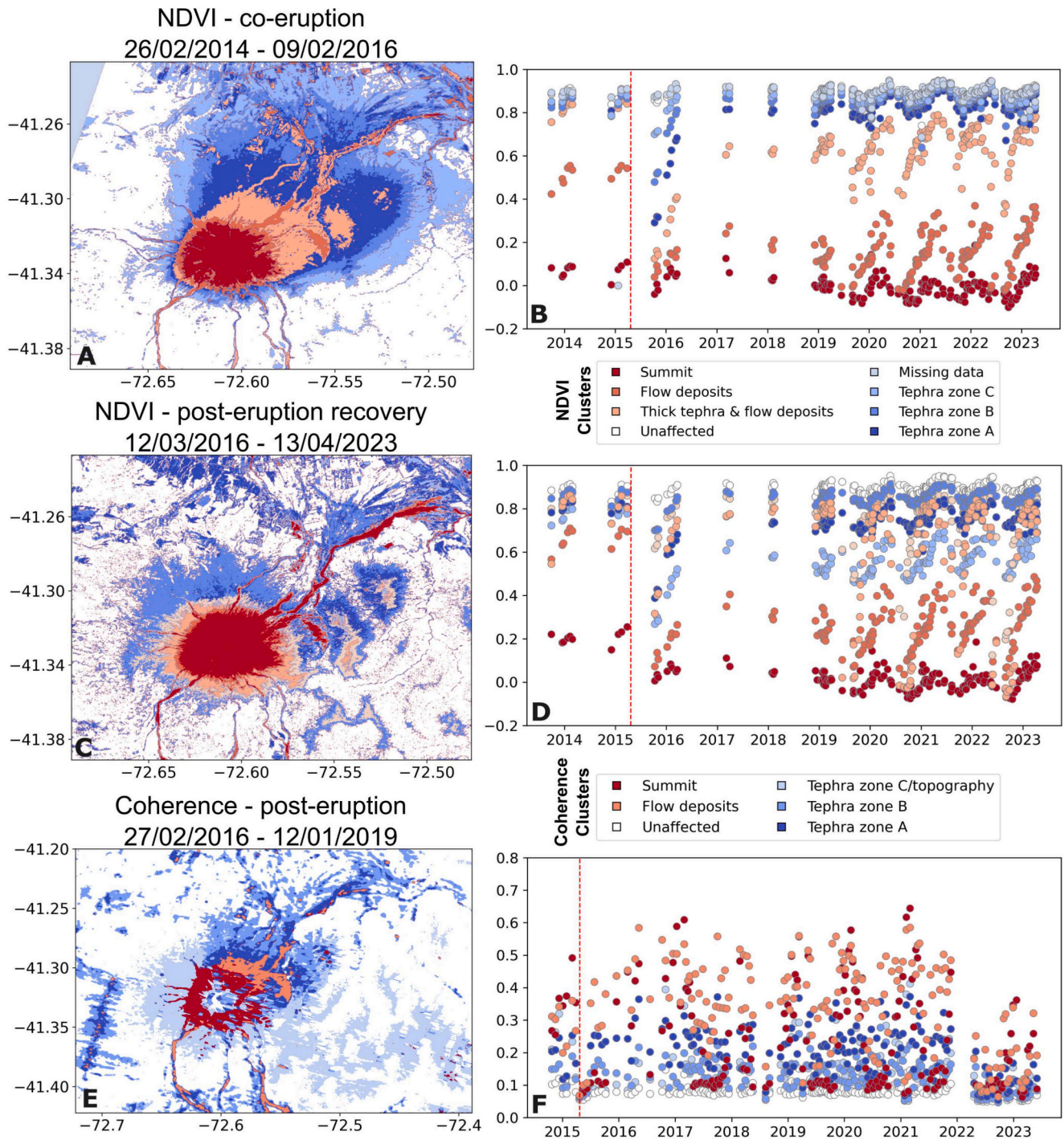


Fig. 6. A) NDVI clustering over the eruptive period (26/02/2014–09/02/2016), producing 8 clusters, B) time series for the median pixel value of the 8 NDVI clusters, c) NDVI clustering over the post-eruption recovery period (12/03/2016–13/04/2023) D) time series for the median pixel of the 8 recovery clusters E) coherence clustering over the post-eruptive period (27/02/2016–12/01/2019) F) time series for the median pixel for the 6 coherence clusters.

changes, the radar imagery complements this by highlighting structural changes and areas of high magnitude impact. As such, using and comparing multiple datasets provides insight and flexibility, especially in cases where one type of data may be limited (e.g. cloud coverage limiting optical image acquisitions).

4.2. Post-eruption forest recovery

Vegetation recovery trends, observable in both the optical and radar datasets, can be linked to the intensity of the eruption impacts and to the

type of vegetation damage. Areas affected by tephra fall began their recovery within 6 months of the eruption, with rapid increases in NDVI occurring in the first few years. This is indicative of vegetation damage rather than death, decreasing with distance from the volcano up to around 20 km, along a gradient defined both by decreasing tephra thickness and coarseness. The lack of extensive zones of increased phase coherence, away from the eroded channels, indicates that trees were not damaged to the extent that the signal became dominated by the more stably scattering forest floor. In contrast, the PDC impacted channels experienced a larger immediate decrease in NDVI and also a much

slower recovery rate, with little evidence for any regrowth in the 5 years immediately post-eruption. This is also clear in the higher phase coherence values in channels over this time. This is consistent with total vegetation loss and burial within these channels (Romero et al., 2023) and with high levels of channel activation (e.g. lahars) and instability persisting for several years, preventing any vegetation recovery. After 2019, the gradual onset of NDVI recovery suggests channel stabilisation and the growth of a sparse successional assemblage, which then exhibits a linear rate of recovery. This period also corresponds to an increase in post-eruption NDVI at the perimeters of the channels (Fig. 7 panel E), showing that initial stages of vegetation recovery develop from channel margins, likely due to the proximity of healthy vegetation and potentially to less extensive initial damage or ongoing rates of erosion. A field campaign undertaken in December 2023 confirmed the regrowth pattern of vegetation at the edges of these channels (Fig. 7). We use NDVI as a way to map channel evolution during and following the eruption. Where channels are marked by vegetation at their edges, satellite NDVI measurements capture initial flow width (including bank erosion and overtopping) and then the gradual narrowing of this damaged region as vegetation recovers post-eruption. Fig. 7 shows a clear decrease in NDVI at the time of eruption across all studied channel transects. In locations also affected by tephra fall, the specific channel impacts are hard to discern, because the NDVI is initially low across the whole transect (Fig. 7 transects 1,2,3), but where there was no tephra deposition (channel 4) the initial impact and recovery patterns are clearly constrained. These transects also highlight changes in active channel patterns driven by the eruption, including a new channel in transect 2 and widening of channels in 1 and 3.

4.3. Vegetation damage as a proxy for tephra thickness

Cluster analysis is advantageous for the classification of vegetation impact and recovery as it utilises the full trajectory of damage and recovery to differentiate between processes (Fig. 6). Clusters of the time series highlight structure in the proximal impact zone and in the PDC

affected channels (Fig. 6) that are harder to discern in the maps of NDVI or coherence change alone. Several of the clusters from the NDVI co-eruption cluster analysis form a concentric sectoral pattern, which we infer to reflect the true shape of tephra-fall deposit isopachs close to the volcano. Although our cluster boundaries are not strictly quantitative indicators of tephra deposit thickness (and the number of boundaries is dependent on our selected discretisation), they mark zones of similar initial damage and similar recovery rate, which we expect to correlate closely with tephra thickness. This interpretation is supported by the very clear spatial correspondence between the axes of the cluster-defined pattern and the observed distribution directions of the two main eruption pulses: the cluster analysis picks out two discrete transport trajectories (at approximately 40° and 65°), with the sector along the southerly axis extending slightly further from the vent, consistent with the larger volume and column height of the second eruptive pulse. This pattern is most clearly evident in the NDVI cluster analysis, on which we base our re-defined isopach distribution, but is also evident in the coherence cluster analysis (Fig. 6 panel E). The spatial pattern of the cluster analysis thus closely corresponds to the expected tephra fall dispersal patterns, and picks out spatial relationships and the impacts of discrete eruptive phases that would simply be unobservable based on the resolution of point-based field measurements. The challenges with producing accurate proximal isopachs based on field measurements is evident in Fig. 8, with a substantial discrepancy between two published proximal isopach patterns, neither of which constrains the spatial form evident in our NDVI cluster analysis. Using our NDVI clusters we re-estimate the tephra deposition isopachs. We calibrate our NDVI cluster-based boundaries against the nearest ground based measurements from Romero et al. (2016), thus assigning an estimated numerical value to each boundary and using this to define revised proximal isopachs. The thinning pattern is consistent for all prior ground based measurements but one (24 cm), which we consider may be an erroneous measurement as it is an outlier in terms of expected thinning trends. Although there is some uncertainty in our approach, the isopach areas that we redefine in this way show a clear exponential thinning rate, as

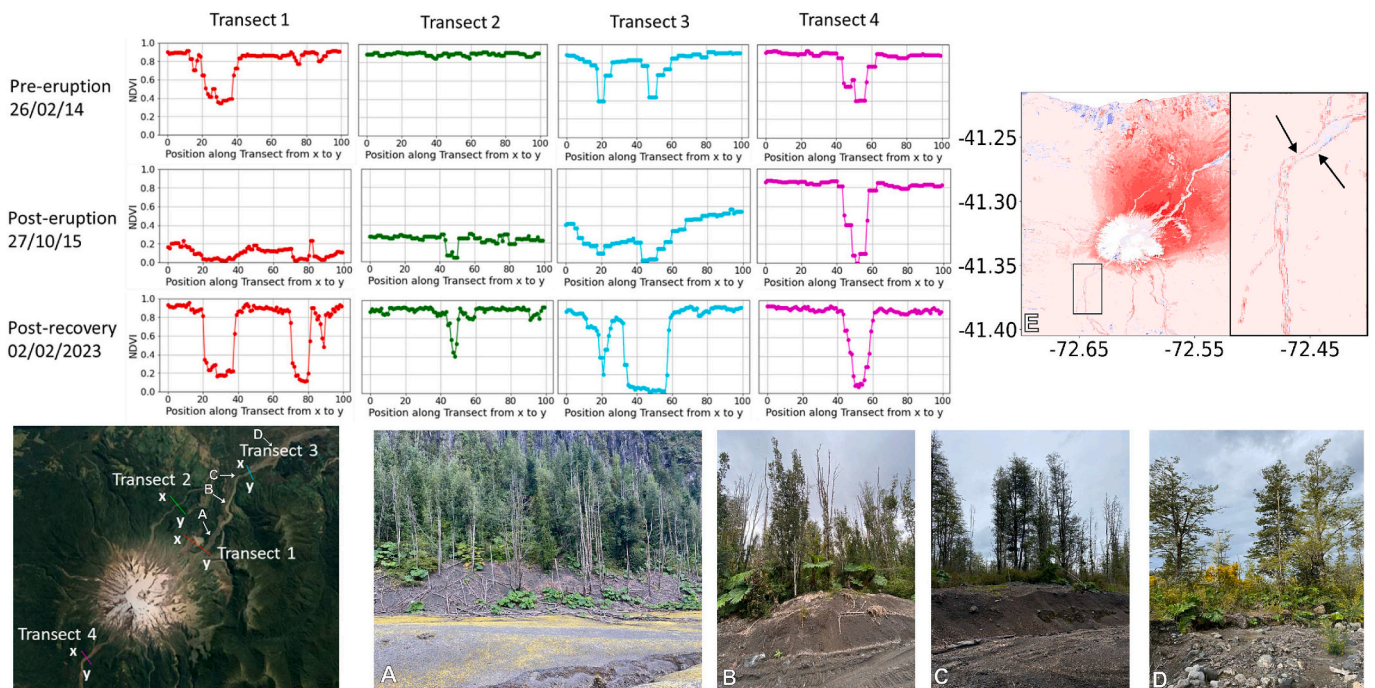


Fig. 7. NDVI transects at different channel locations around Calbuco show the impact of flow deposits on vegetation and how they recover post eruption. Transects 1–4 (locations shown on the Sentinel-2 image) show the changes in NDVI from pre-eruption, 6 months post-eruption and almost 8 years post-eruption. Images A–D show the vegetation at the edges of channels from a field campaign in December 2023. E) Post-eruption NDVI change highlighting the pattern of NDVI increase on the channel perimeters.

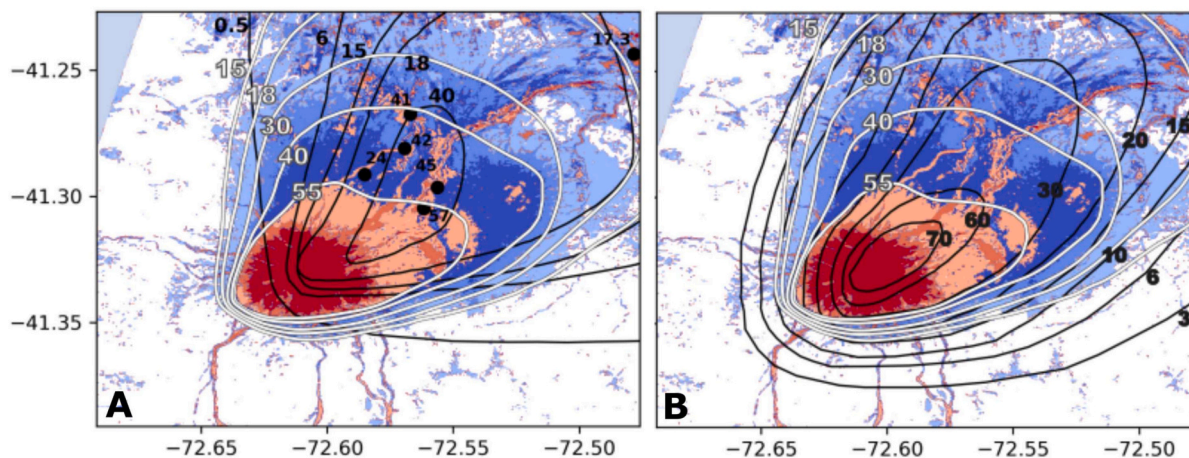


Fig. 8. NDVI clustered eruption impacts overlain with previous eruption isopachs in black and our re-estimated isopachs, from the cluster analysis of NDVI, in white. A) Comparing our re-estimated isopachs with the ash isopachs and field measurements of tephra thickness from [Romero et al. \(2016\)](#) B) Comparing our re-estimated isopachs with isopachs from [Hayes et al. \(2019\)](#).

expected in tephra-fall deposits. This further validates our use of the cluster boundaries as a proxy for fall deposit thickness. By combining our newly defined proximal isopach shapes (15 cm and above) with previous mapping of more distal isopachs, shown in supplementary fig. A.6 (less than 15 cm thickness; from [Romero et al. \(2016\)](#)), we re-estimate the volume of the eruption. Using the method from [Pyle \(1989\)](#) and [Pyle \(1995\)](#), based on two exponential segments, we obtain a re-estimated eruption volume of 0.28 km³, a slightly higher value than the estimate of [Romero et al. \(2016\)](#) of 0.27 km³.

Using NDVI change as a proxy for tephra thickness seems to be effective at Calbuco only for deposits exceeding 15 cm, because thinner tephra deposition did not produce measurable changes in NDVI. The thickness of tephra deposits that produce measurable NDVI changes may vary between eruptions and likely has some dependence on tephra density, grain size and vegetation type. It may also differ substantially between dry and wet tephra deposition. Our observations imply that our method is most useful in the proximal regions of larger magnitude eruptions with extensive tephra deposition. This is nevertheless valuable, because these regions are often forest covered, inaccessible, and

may show the most complex depositional and damage patterns. A significant proportion of deposit volume lies within these proximal regions, and our approach has strong potential for revealing the complexities in eruption impacts in high-damage zones, to complement field-based observations that can be more easily made in distal locations.

Cluster analysis can also provide insights into post-eruption vegetation recovery and how this may be affected by local conditions. Clustering over different time windows, reveals different spatial distributions of NDVI change ([Fig. 6](#) panel C and D), demonstrating that recovery is not only dictated by the initial damage. This is apparent in some regions closer to the vent, where zones impacted by thicker tephra deposits recover to pre-eruption NDVI values more rapidly than regions at a greater distance, with thinner tephra deposits ([Fig. 9](#) Panel A). The areas of slower recovery align with areas of elevated topography (>1000 m) ([Fig. 9](#) and [Fig. 1](#) panel D), suggesting that altitude and slope gradient may be factors that delay forest recovery. It has been shown in previous studies how environmental factors influence vegetation recovery after damage ([Crk et al., 2009](#); [Johnstone et al., 2010](#); [Decker and Boerner, 2003](#); [Ireland and Petropoulos, 2015](#)).

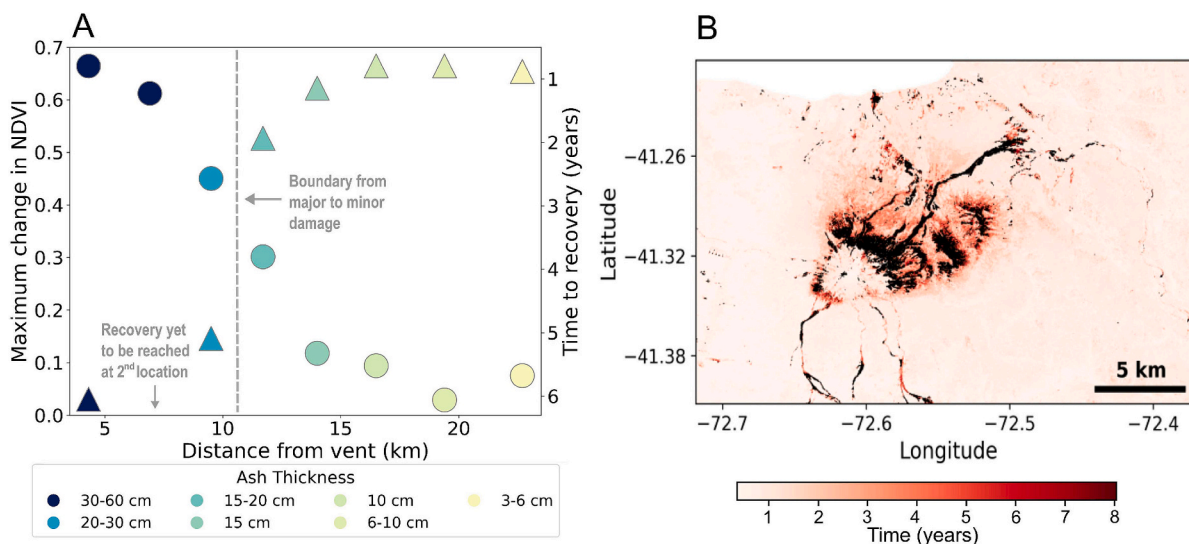


Fig. 9. A) A comparison of vegetation damage vs recovery at increasing distance (decreasing ash thickness), circles show maximum NDVI decrease immediately post-eruption, triangles shows the time to recovery in years for the same areas in [Fig. 3](#). B) The recovery time of NDVI, recovery is defined as being within 1 % of the pre-eruption median value and is calculated on a pixel basis, with darker red being more time to recovery and black pixels being yet to reach the pre-eruption value.

4.4. Link between impact and recovery time

The time taken for vegetation to recover is related to the intensity of the eruption's initial impact. Panel A in Fig. 9 shows maximum NDVI change against recovery time according to distance from the vent and tephra thickness (colour scale). The recovery time is defined as the time when the NDVI value reaches within 1 % of the pre-eruption median. At just over 10 km distance (equal to around 20 cm tephra thickness) the initial change in NDVI is approximately 0.3 and the time to recover is <3 years. Inside this distance, loss of green vegetation is generally greater and recovery times are longer, with some patches of forest that are yet to recover to previous NDVI levels. In addition to local factors, the characteristics of the tephra itself may affect total recovery time. A previous study on the impact of tephra fall on tree ring thickness showed varying amounts of growth loss, possibly due to differing tephra thickness or characteristics (Carlón Allende et al., 2020). This relationship is not necessarily simple and warrants further exploration. Although thicker tephra deposits at Calbuco clearly show a correlation with increased initial damage, this doesn't necessarily impede recovery. Coarse tephra deposits (lapilli) are likely to form a permeable layer that protects the underlying soil and allows water penetration and retention, plausibly benefiting tree recovery. In contrast, finer and thinner ash deposits may be less permeable and promote enhanced runoff and erosion. For the Calbuco eruption, initial damage nevertheless shows a clear correlation with distance and tephra dispersal patterns, suggesting that increased grain size and increased intensity of tephra fallout both led to greater damage. Post-eruption photographs, including a field survey in 2023 (Fig. 7, show that trees throughout the region affected by intense tephra fall remained standing and generally retained their branched form (away from the more intensely damaged zones adjacent to channels). This suggests that initial damage likely involved a combination of tree defoliation and the burial of ground vegetation, perhaps coupled with minor branch breakage, but not extensive branch damage or tree felling. Field observations suggest this was the case even in the areas of highest tephra fallout. This explains the very rapid recovery of areas affected by tephra fall, with mature trees remaining in place and able to re-sprout. Although this may appear surprising, given deposit thicknesses up to half a metre or more, low density pumice lapilli may fall through canopies with relatively limited damage. Had this deposition been wet, or accompanied by rainfall, the impacts and recovery rate may have been quite different, especially in areas affected by finer-grained (ash) deposition. As was observed from extensive mud-rain following the Krakatau eruption in 1883 (Simkin, 1983), wet ash can rapidly coat and load branches, causing extensive breakage and damage at much lower fall deposit thicknesses than occurred at Calbuco. Such processes are likely to strongly influence forest recovery rates and successional patterns, given the impacts on canopy structure.

5. Conclusion

We investigate the use of NDVI, backscatter and coherence to identify forest disturbance and recovery after the 2015 eruption of Calbuco. We analyse time series from all three methods, which show the co-eruptive change and post-eruption recovery. NDVI drops sharply post-eruption due to vegetation loss or damage. The pattern of NDVI loss and recovery shows a bilobate shape that corresponds closely with observed eruption plume dispersal and the intensity of the two main eruption phases, indicating that NDVI can be used as a proxy for tephra distribution. NDVI can also be used to map changes to vegetation at channel boundaries, and therefore their changing extent during and post-eruption. Backscatter increases with the emplacement of eruptive material, and subsequently decreases, although not to pre-eruption values in the most severely impacted areas. The variance in backscatter is significantly larger post-eruption, possibly consistent with a now less homogeneous vegetation cover due to eruption damage. Coherence is lost with the emplacement of material at the eruption

onset, but then increases with the loss of vegetation, particularly in channels and to the north east of the volcano (in the zone most heavily impacted by tephra fall deposition). Both the NDVI and coherence show areas that have not yet fully recovered from the eruption. The detailed pattern of changes in NDVI and coherence can effectively be demonstrated using k-means clustering of multiple acquisitions. Cluster analysis groups pixels with similar time series, and therefore with similar levels of both initial damage and recovery. In NDVI this highlights the tephra fall deposit dispersal patterns in detail, and cluster boundaries can be used as a proxy for tephra isopach distribution (although only in regions of observable NDVI damage, which in this case corresponds to deposit thicknesses over 15 cm). These refined isopachs allow us to re-estimate the eruptive volume at 0.28 km³. This method has strong potential to reveal depositional complexities and eruptive impacts, and to determine eruption volumes, in proximal regions with high levels of damage following large explosive eruptions, and is complementary to more distal field-based datasets. Vegetation recovery rates differ between impact type, based on the initial intensity of the damage. Vegetation recovery occurs mostly in the 3 years following the eruption, but areas with the greatest damage (thickest tephra and channel deposits) take 7 or 8 years to recover, and in some locations are yet to recover, particularly at high elevations and in major channels impacted by PDCs and lahars. We demonstrate that optical and radar satellite data can be used to observe forest disturbance and recovery to understand eruption processes, providing high resolution and quantifiable insights into damage characteristics, deposit distributions and environmental change. This is likely to be of particular value following large explosive eruptions with complex disturbance patterns, and provides a route to determining eruption impacts in vegetated volcanic regions globally.

Declaration of competing interest

The authors declare that they have no known competing financial interests or personal relationships that could have appeared to influence the work reported in this paper.

Data availability

Sentinel-1 imagery is freely available from ESA's Copernicus Open Access Hub. Landsat 8 and Sentinel-2 imagery are freely available and accessed from Google Earth Engine (<https://developers.google.com/earth-engine/datasets/>).

Acknowledgements

MLU is supported by the Natural Environment Research Council (NERC) through a SENSE CDT studentship (grant no. NE/T00939X/1). SKE is funded by NERC IRF (NE/R015546/1) and is a member of the NERC Centre for the Observation and Modelling of Earthquakes, Volcanoes and Tectonics, a partnership between UK Universities and the British Geological Survey. SW acknowledges support from the Birmingham Institute of Forest Research. SW gratefully acknowledges support from the Leverhulme Trust through its Forest Edge Doctoral Scholarship Programme (DS-2017-057). We thank the FONDECYT regular 1200079 project for their contribution of field work. AP is supported by a PhD scholarship granted by Agencia Nacional de Investigación y Desarrollo (ANID) of Chile (Beca Doctorado Nacional No. 21211121).

Appendix A. Supplementary data

Supplementary data to this article can be found online at <https://doi.org/10.1016/j.jvolgeores.2024.108204>.

References

- Askne, J., Dammert, P., Ulander, L., Smith, G., 1997. C-band repeat-pass interferometric SAR observations of the forest. *IEEE Trans. Geosci. Remote Sens.* 35, 25–35. <https://doi.org/10.1109/36.551931> conference Name: IEEE Transactions on Geoscience and Remote Sensing.
- Ayris, P.M., Delmelle, P., 2012. The immediate environmental effects of tephra emission. *Bull. Volcanol.* 74, 1905–1936. <https://doi.org/10.1007/s00445-012-0654-5>.
- Babu, A., Kumar, S., 2019. InSAR coherence and backscatter images based analysis for the Anak Krakatau Volcano Eruption. In: *Proceedings*, 24, p. 21. URL: <https://www.mdpi.com/2504-3900/24/1/21>. <https://doi.org/10.3390/IECG2019-06216>. number: 1 Publisher: Multidisciplinary Digital Publishing Institute.
- Bai, Z.G., Dent, D.L., Olsson, L., Schaeppman, M.E., 2008. Proxy global assessment of land degradation. *Soil Use Manag.* 24, 223–234. <https://doi.org/10.1111/j.1475-2743.2008.00169.x>.
- Balztzer, H., 2001. Forest mapping and monitoring with interferometric synthetic aperture radar (InSAR). *Prog. Phys. Geogr. Earth Environ.* 25, 159–177. <https://doi.org/10.1177/030913330102500201> publisher: SAGE Publications Ltd.
- Bastos, A., Gouveia, C.M., DaCamara, C.C., Trigo, R.M., 2011. Modelling post-fire vegetation recovery in Portugal. *Biogeosciences* 8, 3593–3607. URL: <https://bg.copernicus.org/articles/8/3593/2011/bg-8-3593-2011.html>. <https://doi.org/10.5194/bg-8-3593-2011>. publisher: Copernicus GmbH.
- Biass, S., Jenkins, S.F., Aeberhard, W.H., Delmelle, P., Wilson, T., 2022. Insights into the vulnerability of vegetation to tephra fallout from interpretable machine learning and big Earth observation data. *Nat. Hazards Earth Syst. Sci.* 22, 2829–2855. URL: <https://nhess.copernicus.org/articles/22/2829/2022/>. <https://doi.org/10.5194/nhess-22-2829-2022>. publisher: Copernicus GmbH.
- Biondi, F., Estrada, I.G., Ruiz, J.C.G., Torres, A.E., 2003. Tree growth response to the 1913 eruption of Volcn de Fuego de Colima, Mexico. *Quat. Res.* 59, 293–299. URL: <https://www.cambridge.org/core/journals/quaternary-research/article/abs/tree-growth-response-to-the-1913-eruption-of-volcan-de-fuego-de-colima-mexico/389E2EE1BDDC683535F870B4C185B32> [https://doi.org/10.1016/S0033-5894\(03\)00034-6](https://doi.org/10.1016/S0033-5894(03)00034-6).
- Bonesio, H., Skjelvg, A.O., 1999. Regrowth rates of Timothy and Meadow Fescue cut at five phenological stages. *Acta Agric. Scand. Sect. B - Soil Plant Sci.* 49, 209–215. URL: <http://www.tandfonline.com/doi/abs/10.1080/713782028>. <https://doi.org/10.1080/713782028>.
- Brown, S., Gillespie, A.J.R., Lugo, A.E., 1989. Biomass estimation methods for tropical forests with applications to forest inventory data. *For. Sci.* 35, 881–902. <https://doi.org/10.1093/forestscience/35.4.881>.
- Buitenwerf, R., Sandel, B., Normand, S., Mimet, A., Svenning, J.C., 2018. Land surface greening suggests vigorous woody regrowth throughout European semi-natural vegetation. *Glob. Chang. Biol.* 24, 5789–5801. <https://doi.org/10.1111/gcb.14451>.
- Carey, S., Sigurdsson, H., 1989. The intensity of plinian eruptions. *Bull. Volcanol.* 51, 28–40. <https://doi.org/10.1007/BF01086759>.
- Carlón Allende, T., Macas, J.L., Mendoza, M.E., Villanueva Daz, J., 2020. Evidence of volcanic activity in the growth rings of trees at the Tacaná volcano, Mexico/Guatemala border. *Can. J. For. Res.* 50, 65–72. <https://doi.org/10.1139/cjfr-2019-0214> publisher: NRC Research Press.
- Carlón Allende, T., Macías, J.L., Mendoza, M.E., Díaz, J.V., 2022. Influence of volcanic ash deposits on the radial growth of trees in Central Mexico: the case of Parícutin volcano. *Eur J Forest Res* 141, 605–615. <https://doi.org/10.1007/s10342-022-01463-7>.
- Castruccio, A., Clavero, J., 2015. Lahar simulation at active volcanoes of the Southern Andes: implications for hazard assessment. *Nat. Hazards* 77, 693–716. <https://doi.org/10.1007/s11069-015-1617-x>.
- Castruccio, A., Clavero, J., Segura, A., Samaniego, P., Roche, O., Le Penec, J.L., Droguett, B., 2016. Eruptive parameters and dynamics of the April 2015 sub-Plinian eruptions of Calbuco volcano (southern Chile). *Bull. Volcanol.* 78, 62. <https://doi.org/10.1007/s00445-016-1058-8>.
- Charbonnier, S.J., Germa, A., Connor, C.B., Gertisser, R., Preece, K., Komorowski, J.C., Lavigne, F., Dixon, T., Connor, L., 2013. Evaluation of the impact of the 2010 pyroclastic density currents at Merapi volcano from high-resolution satellite imagery, field investigations and numerical simulations. *J. Volcanol. Geotherm. Res.* 261, 295–315. URL: <https://www.sciencedirect.com/science/article/pii/S0377027313000036>. <https://doi.org/10.1016/j.jvolgeores.2012.12.021>.
- Chen, X., Vogelmann, J.E., Rollins, M., Ohlen, D., Key, C.H., Yang, L., Huang, C., Shi, H., 2011. Detecting post-fire burn severity and vegetation recovery using multi-temporal remote sensing spectral indices and field-collected composite burn index data in a ponderosa pine forest. *Int. J. Remote Sens.* 32, 7905–7927. <https://doi.org/10.1080/01431161.2010.524678>.
- Chou, W.C., Lin, W.T., Lin, C.Y., 2009. Vegetation recovery patterns assessment at landslides caused by catastrophic earthquake: a case study in Central Taiwan. *Environ. Monit. Assess.* 152, 245–257. <https://doi.org/10.1007/s10661-008-0312-8>.
- Crk, T., Uriarte, M., Corsi, F., Flynn, D., 2009. Forest recovery in a tropical landscape: what is the relative importance of biophysical, socioeconomic, and landscape variables? *Landscape Ecol.* 24, 629–642. <https://doi.org/10.1007/s10980-009-9338-8>.
- Dale, V.H., Crisafulli, C.M., Swanson, F.J., 2005a. 25 years of ecological change at Mount St. Helens. *Science* 308, 961–962. <https://doi.org/10.1126/science.1109684> publisher: American Association for the Advancement of Science.
- Dale, V.H., Swanson, F.J., Crisafulli, C.M., 2005b. Disturbance, survival, and succession: Understanding ecological responses to the 1980 eruption of Mount St. Helens. In: Dale, V.H., Swanson, F.J., Crisafulli, C.M. (Eds.), *Ecological Responses to the 1980 Eruption of Mount St. Helens*. Springer, New York, NY, pp. 3–11. https://doi.org/10.1007/0-387-28150-9_1.
- Dale, V.H., Delgado-Acevedo, J., MacMahon, J., 2008. Effects of modern volcanic eruptions on vegetation. In: Marti, J., Ernst, G.G.J. (Eds.), *Volcanoes and the Environment*. Cambridge University Press.
- de Jong, R., Verbesselt, J., Schaepman, M.E., de Bruin, S., 2012. Trend changes in global greening and browning: contribution of short-term trends to longer-term change. *Glob. Chang. Biol.* 18, 642–655. <https://doi.org/10.1111/j.1365-2486.2011.02578.x>.
- De Schutter, A., Kervyn, M., Canters, F., Bosshard-Stadlin, S.A., Songo, M.A.M., Mattsson, H.B., 2015. Ash fall impact on vegetation: a remote sensing approach of the Oldoinyo Lengai 2007/08 eruption. *J. Appl. Volcanol.* 4, 15. <https://doi.org/10.1186/s13617-015-0032-z>.
- Decker, K.L., Boerner, R., 2003. Elevation and vegetation influences on soil properties in Chilean Nothofagus forests. *Rev. Chil. Hist. Nat.* 76. <https://doi.org/10.4067/S0716-078X2003000300003>.
- del Moral, R., Wood, D.M., 1993. Early primary succession on the volcano Mount St. Helens. *J. Veg. Sci.* 4, 223–234. <https://doi.org/10.2307/3236108>.
- Delmelle, P., 2003. Environmental impacts of tropospheric volcanic gas plumes. *Geol. Soc. Lond., Spec. Publ.* 213, 381–399. <https://doi.org/10.1144/GSL.SP.2003.213.01.23> publisher: The Geological Society of London.
- Dorigo, W.A., Zurita-Milla, R., de Wit, A.J.W., Brazile, J., Singh, R., Schaeppman, M.E., 2007. A review on reflective remote sensing and data assimilation techniques for enhanced agroecosystem modeling. *Int. J. Appl. Earth Obs. Geoinf.* 9, 165–193. URL: <https://www.sciencedirect.com/science/article/pii/S0303243406000201>. <https://doi.org/10.1016/j.jag.2006.05.003>.
- Dualeh, E.W., Ebmeier, S.K., Wright, T.J., Albino, F., Naismith, A., Biggs, J., Ordoez, P. A., Boogher, R.M., Roca, A., 2021. Analyzing explosive volcanic deposits from satellite-based radar backscatter, Volcn de Fuego, 2018. *J. Geophys. Res. Solid Earth* 126, e2021JB022250. <https://doi.org/10.1029/2021JB022250>.
- Easdale, M.H., Bruzzone, O., 2018. Spatial distribution of volcanic ash deposits of 2011 Puyehue-Cordón Caulle eruption in Patagonia as measured by a perturbation in NDVI temporal dynamics. *J. Volcanol. Geotherm. Res.* 353, 11–17. URL: <https://www.sciencedirect.com/science/article/pii/S0377027317306017>. <https://doi.org/10.1016/j.jvolgeores.2018.01.020>.
- Ebmeier, S.K., Biggs, J., Mather, T.A., Elliott, J.R., Wadge, G., Amelung, F., 2012. Measuring large topographic change with InSAR: Lava thicknesses, extrusion rate and subsidence rate at Santiaguillo volcano, Guatemala. *Earth Planet. Sci. Lett.* 335–336, 216–225. URL: <https://www.sciencedirect.com/science/article/pii/S0012821X1200194X>. <https://doi.org/10.1016/j.epsl.2012.04.027>.
- Echeverría, C., Coomes, D., Salas, J., Rey-Benayas, J.M., Lara, A., Newton, A., 2006. Rapid deforestation and fragmentation of Chilean Temperate Forests. *Biol. Conserv.* 130, 481–494. URL: <https://www.sciencedirect.com/science/article/pii/S0006320706000358>. <https://doi.org/10.1016/j.biocon.2006.01.017>.
- Evans, D., Farr, T., van Zyl, J., Zebker, H., 1988. Radar polarimetry: analysis tools and applications. *IEEE Trans. Geosci. Remote Sens.* 26, 774–789. <https://doi.org/10.1109/36.7709> conference Name: IEEE Transactions on Geoscience and Remote Sensing.
- Foga, S., Scaramuzza, P.L., Guo, S., Zhu, Z., Dilley, R.D., Beckmann, T., Schmidt, G.L., Dwyer, J.L., Joseph Hughes, M., Laue, B., 2017. Cloud detection algorithm comparison and validation for operational Landsat data products. *Remote Sens. Environ.* 194, 379–390. URL: <https://www.sciencedirect.com/science/article/pii/S0034425717301293>. <https://doi.org/10.1016/j.rse.2017.03.026>.
- Foster, D.R., Knight, D.H., Franklin, J.F., 1998. Landscape patterns and legacies resulting from large, infrequent forest disturbances. *Ecosystems* 1, 497–510. <https://doi.org/10.1007/s100219900046>.
- Franco-Ramos, O., Castillo, M., Muñoz-Salinas, E., 2016. Using tree-ring analysis to evaluate intra-eruptive lahar activity in the Nexpayantla Gorge, Popocatepetl volcano (Central Mexico). *CATENA* 147, 205–215. URL: <https://www.sciencedirect.com/science/article/pii/S0341816216302508>. <https://doi.org/10.1016/j.catena.2016.06.045>.
- Franklin, J.F., 1990. Biological legacies: A Critical management concept from Mount St. Helens. In: *Trans. North American Wildlands Natural Resource Conference*, 55, pp. 216–219.
- Franklin, J.F., Lindenmayer, D., MacMahon, J.A., McKee, A., Magnuson, J., Perry, D.A., Waide, R., Foster, D., 2000. There are immense differences between even-aged silvicultural disturbances (especially clearcutting) and natural disturbances, such as windthrow, wildfire, and even volcanic eruptions. *Conserv. Pract.* 1, 8–17. <https://doi.org/10.1111/j.1526-4629.2000.tb00155>.
- Gerlach, T.M., Doukas, M.P., McGee, K.A., Kessler, R., 2001. Soil efflux and total emission rates of magmatic CO₂ at the Horseshoe Lake tree kill, Mammoth Mountain, California, 1995/1999. *Chem. Geol.* 177, 101–116. URL: <https://www.sciencedirect.com/science/article/pii/S0009254100003855>. [https://doi.org/10.1016/S0009-2541\(00\)00385-5](https://doi.org/10.1016/S0009-2541(00)00385-5).
- Gillman, L.N., Wright, S.D., Cusens, J., McBride, P.D., Malhi, Y., Whittaker, R.J., 2015. Latitude, productivity and species richness. *Glob. Ecol. Biogeogr.* 24, 107–117. <https://doi.org/10.1111/geb.12245>.
- Global Volcanism Programme, 2015. Report on Calbuco (Chile). In: *Venzke, E. (Ed.), Bulletin of the Global Volcanism Network*, 40. Smithsonian Institution, p. 6. <https://doi.org/10.5479/si.GVP.BGVN201506-358020>.
- Goetz, S.J., Fiske, G.J., Bunn, A.G., 2006. Using satellite time-series data sets to analyze fire disturbance and forest recovery across Canada. *Remote Sens. Environ.* 101,

- 352–365. URL <https://www.sciencedirect.com/science/article/pii/S0034425706000289>. <https://doi.org/10.1016/j.rse.2006.01.011>.
- Gouveia, C., Trigo, R.M., DaCamara, C.C., 2009. Drought and vegetation stress monitoring in Portugal using satellite data. *Nat. Hazards Earth Syst. Sci.* 9, 185–195. URL <https://nhess.copernicus.org/articles/9/185/2009/>. <https://doi.org/10.5194/nhess-9-185-2009>. publisher: Copernicus GmbH.
- Gouveia, C., DaCamara, C.C., Trigo, R.M., 2010. Post-fire vegetation recovery in Portugal based on spot/vegetation data. *Nat. Hazards Earth Syst. Sci.* 10, 673–684. <https://doi.org/10.5194/nhess-10-673-2010> publisher: Copernicus GmbH.
- Grilli, S.T., Tappin, D.R., Carey, S., Watt, S.F.L., Ward, S.N., Grilli, A.R., Engwell, S.L., Zhang, C., Kirby, J.T., Schambach, L., Muin, M., 2019. Modelling of the tsunami from the December 22, 2018 lateral collapse of Anak Krakatau volcano in the Sunda Straits, Indonesia. *Sci. Rep.* 9, 11946. URL <https://www.nature.com/articles/s41598-019-48327-6>. <https://doi.org/10.1038/s41598-019-48327-6>. number: 1 Publisher: Nature Publishing Group.
- Grishin, S.Y., del Moral, R., Krestov, P.V., Verkholt, V.P., 1996. Succession following the catastrophic eruption of Ksudach volcano (Kamchatka, 1907). *Vegetatio* 127, 129–153. <https://doi.org/10.1007/BF00044637>.
- Hanssen, R.F., 2001. *Radar Interferometry: Data Interpretation and Error Analysis*. Springer, Netherlands, Dordrecht, NETHERLANDS, THE. URL <http://ebookcentral.proquest.com/lib/leeds/detail.action?docID=6487976>.
- Hayes, J., Deligne, N., Bertin, L., Calderon, R., Wardman, J., Wilson, T., Leonard, G., Stewart, C., Wallace, K., Baxter, P., 2019. Impacts of the 2015 Eruption of Calbuco Volcano on Chilean Infrastructure, Utilities, Agriculture, and Health. *GNS Science, Lower Hutt, New Zealand*. <https://doi.org/10.21420/02YC-VX66>.
- Head, E.M., Maclean, A.L., Carn, S.A., 2012. Mapping lava flows from Nyamuragira volcano (19672011) with satellite data and automated classification methods. *Geomat. Nat. Haz. Risk* 4, 119144. <https://doi.org/10.1080/19475705.2012.680503>.
- Ireland, G., Petropoulos, G.P., 2015. Exploring the relationships between post-fire vegetation regeneration dynamics, topography and burn severity: a case study from the Montane Cordillera Ecozones of Western Canada. *Appl. Geogr.* 56, 232–248. URL <https://linkinghub.elsevier.com/retrieve/pii/S0143622814002719>. <https://doi.org/10.1016/j.apgeog.2014.11.016>.
- Jacquemoud, S., Baret, F., 1990. PROSPECT: a model of leaf optical properties spectra. *Remote Sens. Environ.* 34, 75–91. URL <https://www.sciencedirect.com/science/article/pii/003442579090100Z>. [https://doi.org/10.1016/0034-4257\(90\)90100-Z](https://doi.org/10.1016/0034-4257(90)90100-Z).
- Johnstone, J.F., McIntire, E.J.B., Pedersen, E.J., King, G., Pisaric, M.J.F., 2010. A sensitive slope: estimating landscape patterns of forest resilience in a changing climate. *Ecosphere* 1. <https://doi.org/10.1890/ES10-00102.1> art14.
- Jung, J., Kim, D.J., Laval, M., Yun, S.H., 2016. Coherent change detection using InSAR temporal decorrelation model: a case study for volcanic ash detection. *IEEE Trans. Geosci. Remote Sens.* 54, 5765–5775. <https://doi.org/10.1109/TGRS.2016.2572166> conference Name: IEEE Transactions on Geoscience and Remote Sensing.
- Just, D., Bamler, R., 1994. Phase statistics of interferograms with applications to synthetic aperture radar. *Appl. Opt.* 33, 4361–4368. URL <https://opg.optica.org/ao/abstract.cfm?uri=ao-33-20-4361>. <https://doi.org/10.1364/AO.33.004361>. publisher: Optica Publishing Group.
- Kim, Y., Jackson, T., Bindlish, R., Lee, H., Hong, S., 2012. Radar vegetation index for estimating the vegetation water content of rice and soybean. *IEEE Geosci. Remote Sens. Lett.* 9, 564–568. <https://doi.org/10.1109/LGRS.2011.2174772> conference Name: IEEE Geoscience and Remote Sensing Letters.
- Lai, R., Oguchi, T., Zhong, C., 2022. Evaluating spatiotemporal patterns of post-eruption vegetation recovery at Unzen Volcano, Japan, from landsat time series. *Remote Sens.* 14, 5419. URL <https://www.mdpi.com/2072-4292/14/21/5419>. <https://doi.org/10.3390/rs14215419>.
- Lee, J.S., Grunes, M.R., Kwok, R., 1994. Classification of multi-look polarimetric SAR imagery based on complex Wishart distribution. *Int. J. Remote Sens.* 15, 2299–2311 publisher: Taylor & Francis eprint. <https://doi.org/10.1080/01431169408954244>.
- Li, L., Bakelants, L., Solana, C., Canters, F., Kervyn, M., 2018. Dating lava flows of tropical volcanoes by means of spatial modeling of vegetation recovery. *Earth Surf. Process. Landf.* 43, 840–856. <https://doi.org/10.1002/esp.4284>.
- Likas, A., Vlassis, N., Verbeek, J., 2003. The global k-means clustering algorithm. *Pattern Recogn.* 36, 451–461. URL <https://linkinghub.elsevier.com/retrieve/pii/S0031320302000602>. [https://doi.org/10.1016/S0031-3203\(02\)00060-2](https://doi.org/10.1016/S0031-3203(02)00060-2).
- Lowenstern, J.B., Bleick, H., Vazquez, J.A., Castro, J.M., Larson, P.B., 2012. Degassing of Cl, F, Li, and Be during extrusion and crystallization of the rhyolite dome at Volcán Chaitin, Chile during 2008 and 2009. *Bull. Volcanol.* 74, 2303–2319. <https://doi.org/10.1007/s00445-012-0663-4>.
- Lu, T., Zeng, H., Luo, Y., Wang, Q., Shi, F., Sun, G., Wu, Y., Wu, N., 2012. Monitoring vegetation recovery after China's May 2008 Wenchuan earthquake using Landsat TM time-series data: a case study in Mao County. *Ecol. Res.* 27, 955–966. <https://doi.org/10.1007/s11284-012-0976-y>.
- Macorps, E., Jo, M., Osmanoglu, B., Albayrak, R.A., 2023. Mapping areas impacted by volcanic flows during an eruption using synthetic aperture radar and optical imagery. In: *The International Archives of the Photogrammetry, Remote Sensing and Spatial Information Sciences XLVIII-M-1-2023*, pp. 175–182. URL <https://isprs-archives.copernicus.org/articles/XLVIII-M-1-2023/175/2023/isprs-archives-XLVIII-M-1-2023-175-2023.html>. <https://doi.org/10.5194/isprs-archives-XLVIII-M-1-2023-175-2023>. conference Name: 39th International Symposium on Remote Sensing of Environment (ISRSE-39) From Human needs to SDGs – 24-28 April 2023, Antalya, Trkiye Publisher: Copernicus GmbH.
- Main-Knoorn, M., Pflug, B., Louis, J., Debaecker, V., Mller-Wilm, U., Gascon, F., 2017. Sen2Cor for Sentinel-2. In: *Image and Signal Processing for Remote Sensing XXIII*. SPIE, pp. 37–48. <https://doi.org/10.1117/12.2278218>.
- Major, J.J., Lara, L.E., 2013. Overview of Chaitin Volcano, Chile, and its 2008–2009 eruption. *Andean Geol.* 40, 196–215. URL <http://www.andeangeology.cl/index.php/revista/article/view/V40n2-a01>. <https://doi.org/10.5027/andgeoV40n2-a01>. number: 2.
- Martin, R.S., Watt, S.F.L., Pyle, D.M., Mather, T.A., Matthews, N.E., Georg, R.B., Day, J. A., Fairhead, T., Witt, M.L.L., Quayle, B.M., 2009. Environmental effects of ashfall in Argentina from the 2008 Chaitin volcanic eruption. *J. Volcanol. Geotherm. Res.* 184, 462–472. URL <https://www.sciencedirect.com/science/article/pii/S037702730900184X>. <https://doi.org/10.1016/j.jvolgeores.2009.04.010>.
- Marzen, L.J., Szantoi, Z., Harrington, L.M., Harrington, J.A., 2011. Implications of management strategies and vegetation change in the Mount St. Helens blast zone. *Geocarto Int.* 26, 359–376. <https://doi.org/10.1080/10106049.2011.584977>.
- Matsushita, B., Yang, W., Chen, J., Onda, Y., Qiu, G., 2007. Sensitivity of the enhanced vegetation index (EVI) and normalized difference vegetation index (NDVI) to topographic effects: a case study in high-density cypress forest. *Sensors* 7, 2636–2651. URL <https://www.mdpi.com/1424-8220/7/11/2636>. <https://doi.org/10.3390/s7112636> (number: 11 Publisher: Molecular Diversity Preservation International).
- Mella, M., Roa, H., Vergs, A., Quiroz, D., Bertin, L., Basualto, D., Bertin, D., Garrido, N., 2015. *Productos volcnicos e impactos asociados al ciclo eruptivo del 2015 del volcn Calbuco*.
- Meyer, F.J., McAlpin, D.B., Gong, W., Ajadi, O., Arko, S., Webley, P.W., Dehn, J., 2015. Integrating SAR and derived products into operational volcano monitoring and decision support systems. *ISPRS J. Photogramm. Remote Sens.* 100, 106–117. URL <https://www.sciencedirect.com/science/article/pii/S0924271614001270>. <https://doi.org/10.1016/j.isprsjprs.2014.05.009>.
- Michener, W.K., Houhoulis, P.F., 1997. Detection of vegetation changes associated with extensive flooding in a forested ecosystem. *Photogramm. Eng. Remote Sens.* 12.
- Mitchard, E.T.A., Saatchi, S.S., Woodhouse, I.H., Nangendo, G., Ribeiro, N.S., Williams, M., Ryan, C.M., Lewis, S.L., Feldpausch, T.R., Meir, P., 2009. Using satellite radar backscatter to predict above-ground woody biomass: a consistent relationship across four different African landscapes. *Geophys. Res. Lett.* 36. <https://doi.org/10.1029/2009GL040692>.
- Myneni, R.B., Hall, F.G., Sellers, P.J., Marshak, A.L., 1995. The interpretation of spectral vegetation indexes. *IEEE Trans. Geosci. Remote Sens.* 33, 481–486. <https://doi.org/10.1109/TGRS.1995.8746029> conference Name: IEEE Transactions on Geoscience and Remote Sensing.
- Olson, D.M., Dinerstein, E., Wikramanayake, E.D., Burgess, N.D., Powell, G.V.N., Underwood, E.C., D'amico, J.A., Itoua, I., Strand, H.E., Morrison, J.C., Loucks, C.J., Allnutt, T.F., Ricketts, T.H., Kura, Y., Lamoreux, J.F., Wettengel, W.W., Hedao, P., Kassem, K.R., 2001. Terrestrial ecoregions of the world: a new map of life on earth. *BioScience* 51, 933. URL <https://academic.oup.com/bioscience/article/51/11/933-938/227116>. [https://doi.org/10.1641/0006-3568\(2001\)051\[0933:TEOTWA\]2.0.CO;2](https://doi.org/10.1641/0006-3568(2001)051[0933:TEOTWA]2.0.CO;2).
- Peel, M.C., Finlayson, B.L., McMahon, T.A., 2007. Updated world map of the Koppen-Geiger climate classification. *Hydrol. Earth Syst. Sci.* 12.
- Pyle, D.M., 1989. The thickness, volume and grainsize of tephra fall deposits. *Bull. Volcanol.* 51, 1–15. <https://doi.org/10.1007/BF01086757>.
- Pyle, D.M., 1995. Assessment of the minimum volume of tephra fall deposits. *Journal of Volcanology and Geothermal Research* 69, 379–382. URL <https://www.sciencedirect.com/science/article/pii/0377027395000380>. [https://doi.org/10.1016/0377-0273\(95\)00038-0](https://doi.org/10.1016/0377-0273(95)00038-0).
- Romero, J.E., Morgavi, D., Arzilli, F., Daga, R., Caselli, A., Reckziegel, F., Viramonte, J., Daz-Alvarado, J., Polacci, M., Burton, M., Perugini, D., 2016. Eruption dynamics of the 2223 April 2015 Calbuco Volcano (Southern Chile): analyses of tephra fall deposits. *J. Volcanol. Geotherm. Res.* 317, 15–29. URL <https://www.sciencedirect.com/science/article/pii/S037702731630004X>. <https://doi.org/10.1016/j.jvolgeores.2016.02.027>.
- Romero, J.E., Swanson, F.J., Jones, J.A., Morgavi, D., Giordano, G., Trolese, M., Aguilera, F., Izquierdo, T., Perugini, D., 2023. The April 2015 Calbuco eruption pyroclastic density currents: deposition, impacts on woody vegetation, and cooling on the northern flank of the cone. *Andean Geol.* 50, 319–345. URL <http://www.andeangeology.cl/index.php/revista/article/view/V50n3-3650>. <https://doi.org/10.5027/andgeoV50n3-3650>. number: 3.
- Roy, D., Boschetti, L., Trigg, S., 2006. Remote sensing of fire severity: assessing the performance of the normalized burn ratio. *IEEE Geosci. Remote Sens. Lett.* 3, 112–116. URL <https://ieeexplore.ieee.org/abstract/document/1576701>. <https://doi.org/10.1109/LGRS.2006.5858485>. conference Name: IEEE Geoscience and Remote Sensing Letters.
- Santin-Janin, H., Garel, M., Chapuis, J.L., Pontier, D., 2009. Assessing the performance of NDVI as a proxy for plant biomass using non-linear models: a case study on the Kerguelen archipelago. *Polar Biol.* 32, 861–871. <https://doi.org/10.1007/s00300-009-0586-5>.
- Seiler, R., Hajdas, I., Saurer, M., Houli, N., D'Arrigo, R., Kirchner, J.W., Cherubini, P., 2021. Tree-ring stable isotopes and radiocarbon reveal pre- and post-eruption effects of volcanic processes on trees on Mt. Etna (Sicily, Italy). *Ecology* 14, e2340. <https://doi.org/10.1002/eco.2340>.

- Self, S., 2006. The effects and consequences of very large explosive volcanic eruptions. *Philos. Trans. R. Soc. A Math. Phys. Eng. Sci.* 364, 2073–2097. <https://doi.org/10.1098/rsta.2006.1814> publisher: Royal Society.
- Simkin, T., 1983. Krakatau, 1883: The Volcanic Eruption and its Effects. Books by Alumni. URL: <https://works.swarthmore.edu/alum-books/2974>.
- Small, D., 2011. Flattening gamma: radiometric terrain correction for SAR imagery. *IEEE Trans. Geosci. Remote Sens.* 49, 3081–3093. <https://doi.org/10.1109/TGRS.2011.2120616> conference Name: IEEE Transactions on Geoscience and Remote Sensing.
- Smathers, G.A., Mueller-Dombois, D., 1972. *Invasion and Recovery of Vegetation after a Volcanic Eruption in Hawaii*. Department of Botany, University of Hawaii. Google-Books-ID: 2c89AAAAIAAJ.
- Smith, W.H., 1981. Air pollution and forests: Interactions between air contaminants and forest ecosystems. In: *Springer Series on Environmental Management*. Springer-Verlag, New York.
- Song, C., 2013. Optical remote sensing of forest leaf area index and biomass. *Prog. Phys. Geogr. Earth Environ.* 37, 98–113. <https://doi.org/10.1177/0309133312471367> publisher: SAGE Publications Ltd.
- Swanson, F., Major, J., 2005. Physical events, environments, and geological ecological interactions at Mount St. Helens: March 1980–2004. In: *Ecological Responses to the 1980 Eruption of Mount St. Helens*. Springer New York, NY, pp. 27–44. https://doi.org/10.1007/0-387-28150-9_3.
- Swanson, F.J., Jones, J.A., Crisafulli, C.M., Lara, A., 2013. Effects of volcanic and hydrologic processes on forest vegetation: Chaitin Volcano, Chile. *Andean Geol.* 40, 359–391. URL: <http://www.andeangeology.cl/index.php/revista1/article/view/V40n2-a10>. <https://doi.org/10.5027/andgeo.V40n2-a10>. number: 2.
- Teltscher, K., Fassnacht, F.E., 2018. Using multispectral landsat and sentinel-2 satellite data to investigate vegetation change at Mount St. Helens since the great volcanic eruption in 1980. *J. Mt. Sci.* 15, 1851–1867. <https://doi.org/10.1007/s11629-018-4869-6>.
- Tian, F., Fensholt, R., Verbesselt, J., Grogan, K., Horion, S., Wang, Y., 2015. Evaluating temporal consistency of long-term global NDVI datasets for trend analysis. *Remote Sens. Environ.* 163, 326–340. URL: <https://www.sciencedirect.com/science/article/pii/S0034425715001285>. <https://doi.org/10.1016/j.rse.2015.03.031>.
- Torres, R., Snoeij, P., Geudtner, D., Bibby, D., Davidson, M., Attema, E., Potin, P., Rommen, B., Flourey, N., Brown, M., Traver, I.N., Deghaye, P., Duesmann, B., Rosich, B., Miranda, N., Bruno, C., L'Abbate, M., Croci, R., Pietropaolo, A., Huchler, M., Rostan, F., 2012. GMES Sentinel-1 mission. *Remote Sens. Environ.* 120, 9–24. URL: <https://www.sciencedirect.com/science/article/pii/S0034425712000600>. <https://doi.org/10.1016/j.rse.2011.05.028>.
- Treuhaf, R.N., Madsen, S.N., Moghaddam, M., Zyl, J.J.V., 1996. Vegetation characteristics and underlying topography from interferometric radar. *Radio Sci.* 31, 1449–1485. <https://doi.org/10.1029/96RS01763> conference Name: Radio Science.
- Turner, M.G., Dale, V.H., Everham, E.H., 1997. Fires, hurricanes, and volcanoes: comparing large disturbances. *BioScience* 47, 758–768. URL: <https://www.jstor.org/stable/1313098>. <https://doi.org/10.2307/1313098> publisher: [American Institute of Biological Sciences, Oxford University Press].
- Van Eaton, A.R., Bertin, D., Mastin, L.G., Giacosa, R.E., Gonzlez, J., Valderrama, O., Fontijn, K., Behnke, S.A., 2016. Volcanic lightning and plume behavior reveal evolving hazards during the April 2015 eruption of Calbuco volcano, Chile. *Geophys. Res. Lett.* 43, 3563–3571. <https://doi.org/10.1002/2016GL068076>.
- Veloso, A., Mermoz, S., Bouvet, A., Le Toan, T., Planells, M., Dejoux, J.F., Ceschia, E., 2017. Understanding the temporal behavior of crops using Sentinel-1 and Sentinel-2-like data for agricultural applications. *Remote Sens. Environ.* 199, 415–426. URL: <https://www.sciencedirect.com/science/article/pii/S0034425717303309>. <https://doi.org/10.1016/j.rse.2017.07.015>.
- Veraverbeke, S., Gitas, I., Katagis, T., Polychronaki, A., Somers, B., Goossens, R., 2012. Assessing post-fire vegetation recovery using rednear infrared vegetation indices: accounting for background and vegetation variability. *ISPRS J. Photogramm. Remote Sens.* 68, 28–39. URL: <https://www.sciencedirect.com/science/article/pii/S09242716111001614> <https://doi.org/10.1016/j.isprsjprs.2011.12.007>.
- Vermote, E., Justice, C., Claverie, M., Franch, B., 2016. Preliminary analysis of the performance of the Landsat 8/OLI land surface reflectance product. *Remote Sens. Environ.* 185, 46–56. URL: <https://www.sciencedirect.com/science/article/pii/S0034425716301572>. <https://doi.org/10.1016/j.rse.2016.04.008>.
- Viedma, O., Meli, J., Segarra, D., Garcia-Haro, J., 1997. Modeling rates of ecosystem recovery after fires by using landsat TM data. *Remote Sens. Environ.* 61, 383–398. URL: <https://www.sciencedirect.com/science/article/pii/S0034425797000485>. [https://doi.org/10.1016/S0034-4257\(97\)00048-5](https://doi.org/10.1016/S0034-4257(97)00048-5).
- Werner, C., Wegmiller, U., Strozzi, T., Wiesmann, A., 2000. *Gamma Sar and Interferometric Processing Software*.
- Werner, C., Schmid, M., Ehlers, T.A., Fuentes-Espoz, J.P., Steinkamp, J., Forrest, M., Liakka, J., Maldonado, A., Hickler, T., 2018. Effect of changing vegetation and precipitation on denudation part 1: predicted vegetation composition and cover over the last 21 thousand years along the Coastal Cordillera of Chile. *Earth Surf. Dyn.* 6, 829–858. URL: <https://esurf.copernicus.org/articles/6/829/2018/>. <https://doi.org/10.5194/esurf-6-829-2018>. publisher: Copernicus GmbH.
- Wilson, T.M., Cole, J.W., Stewart, C., Cronin, S.J., Johnston, D.M., 2011. Ash storms: impacts of wind-remobilised volcanic ash on rural communities and agriculture following the 1991 Hudson eruption, southern Patagonia, Chile. *Bull. Volcanol.* 73, 223–239. <https://doi.org/10.1007/s00445-010-0396-1>.
- Wilson, T., Stewart, C., Bickerton, H., Baxter, P., Outes, A.V., Villarosa, G., Rovere, E., 2013. Impacts of the June 2011 Puyehue-Cordón Caulle volcanic complex eruption on urban infrastructure, agriculture and public health. *Inst. Geol. Nuclear Sci.* 20, 1–88. URL: <https://ri.conicet.gov.ar/handle/11336/78121>. accepted: 2019–06–12T19:27:36Z ISSN: 1177–2425.
- Wilson, T.M., Jenkins, S., Stewart, C., 2015. Chapter 3 - Impacts from volcanic ash fall. In: Shroder, J.F., Papale, P. (Eds.), *Volcanic Hazards, Risks and Disasters*, Hazards and Disasters Series. Elsevier, Boston, pp. 47–86. URL: <https://www.sciencedirect.com/science/article/pii/B9780123964533000034>. <https://doi.org/10.1016/B978-0-12-396453-3.00003-4>.
- Woodhouse, I.H., 2017. *Introduction to Microwave Remote Sensing*. CRC Press, Boca Raton. <https://doi.org/10.1201/9781315272573>.
- Yagüe-Martínez, N., Prats-Iraola, P., Rodríguez González, F., Brcic, R., Shau, R., Geudtner, D., Eineder, M., Bamler, R., 2016. Interferometric processing of Sentinel-1 TOPS data. *IEEE Trans. Geosci. Remote Sens.* 54, 2220–2234. <https://doi.org/10.1109/TGRS.2015.2497902> conference Name: IEEE Transactions on Geoscience and Remote Sensing.
- Zebker, H., Villasenor, A.J., Zebker, H.A., Zebker, H.A., 1992. *Decorrelation in Interferometric Radar Echoes*.
- Zobel, D.B., Antos, J.A., 1997. A decade of recovery of understory vegetation buried by volcanic Tephra from Mount St. Helens. *Ecol. Monogr.* 67, 317–344. [https://doi.org/10.1890/0012-9615\(1997\)067\[0317:ADOROU\]2.0.CO;2](https://doi.org/10.1890/0012-9615(1997)067[0317:ADOROU]2.0.CO;2).